frontiers | Frontiers in Physics

TYPE Review
PUBLISHED 06 February 2025
DOI 10.3389/fphy.2024.1531475

OPEN ACCESS

EDITED BY
Masayuki Matsuzaki,
Fukuoka University of Education, Japan

REVIEWED BY
Tomoyuki Maruyama,
Nihon University, Japan
Anto Sulaksono,
University of Indonesia, Indonesia

*CORRESPONDENCE
Tsuyoshi Miyatsu,
tsuyoshi.miyatsu@ssu.ac.kr

RECEIVED 20 November 2024
ACCEPTED 11 December 2024
PUBLISHED 06 February 2025

CITATION
Miyatsu T, Cheoun M-K, Kim K and Saito K (2025) Novel features of asymmetric nuclear matter from terrestrial experiments and astrophysical observations of neutron stars. *Front. Phys.* 12:1531475. doi: 10.3389/fphy.2024.1531475

Novel features of asymmetric nuclear matter from terrestrial experiments and astrophysical observations of neutron stars

Tsuyoshi Miyatsu [1]*, Myung-Ki Cheoun [1], Kyungsik Kim [2] and Koichi Saito [3]

[1]Department of Physics and Origin of Matter and Evolution of Galaxies Institute, Soongsil University, Seoul, Republic of Korea, [2]School of Liberal Arts and Sciences, Korea Aerospace University, Goyang, Republic of Korea, [3]Department of Physics and Astronomy, Faculty of Science and Technology, Tokyo University of Science, Noda, Japan

The accurate measurement of neutron skin thickness of ^{208}Pb by the PREX Collaboration suggests a large value of the nuclear symmetry energy slope parameter, L, whereas the smaller L is preferred to account for the small neutron-star radii from NICER observations. To resolve this discrepancy between nuclear experiments and astrophysical observations, new effective interactions have been developed using relativistic mean-field models with the isoscalar- and isovector-meson mixing. We investigate the effects of δ-nucleon coupling and σ–δ mixing on the ground-state properties of finite nuclei, as well as the characteristics of isospin-asymmetric nuclear matter and neutron stars. Additionally, we explore the role of the quartic ρ-meson self-interaction in dense nuclear matter to mitigate the stiff equation of state for neutron stars resulting from the large δ-nucleon coupling. It is found that the nuclear symmetry energy undergoes a sudden softening at approximately twice the saturation density of nuclear matter, taking into account the PREX-2 result, the recent NICER observation of PSR J0437–4715, and the binary neutron star merger, GW170817.

KEYWORDS

isospin-asymmetric nuclear matter, neutron skin thickness, neutron stars, NICER, nuclear equation of state, nuclear symmetry energy, PREX-2, relativistic mean-field models

1 Introduction

The astrophysical phenomena concerning compact stars as well as the characteristics of finite nuclei and nuclear matter are determined by the nuclear equation of state (EoS), characterized by the relation between the energy density and pressure of the system [1, 2]. Many nuclear EoSs have been contemplated so far through realistic nuclear models in a non-relativistic or relativistic framework [3, 4]. Relativistic mean-field (RMF) calculations, based on the one-boson exchange potential for nuclear interactions [5, 6], have achieved great success in understanding of the properties of nuclear matter and finite nuclei [7]. To reproduce a reasonable nuclear incompressibility and properties of unstable nuclei, the RMF models have been developed by introducing the non-linear self-couplings of isoscalar, Lorentz-scalar (σ) and Lorentz-vector (ω^{μ}) mesons [8, 9]. In addition, the isovector, Lorentz-vector ($\boldsymbol{\rho}^{\mu}$) meson and its non-linear couplings have been considered to describe a neutron skin thickness

of heavy nuclei and characteristics of isospin-asymmetric nuclear matter [10, 11]. The RMF approach is, at present, one of the most powerful tools to study neutron star physics [12–14], as in the case of the Skyrme energy density functional [15–18].

The nuclear symmetry energy, $E_{\rm sym}$, which is defined as the difference between the energies of pure neutron and symmetric nuclear matter, is recognized to be an important physical quantity to study the properties of isospin-asymmetric nuclear EoS [19, 20]. In addition, the slope parameter of nuclear symmetry energy, L, gives a significant constraint on the density dependence of $E_{\rm sym}$ and is related to the neutron skin thickness of heavy nuclei [21]. Laboratory experiments have been also performed to investigate the properties of low-density nuclear matter and to impose constraints on $E_{\rm sym}$ and L through the heavy-ion collisions (HICs) [22, 23]. Recently, the impacts of the higher-order coefficients—the curvature and skewness of nuclear symmetry energy, $K_{\rm sym}$ and $J_{\rm sym}$—have been studied in light of some astrophysical observations, for instance the mass-radius relations of neutron stars and the cooling process of proto-neutron stars [24–26].

Owing to the precise observations of neutron stars, such as the Shapiro delay measurement of a binary millisecond pulsar J1614–2230 [27, 28] and the radius measurement of PSR J0740+6620 from Neutron Star Interior Composition Explorer (NICER) and from X-ray Multi-Mirror (XMM-Newton) Data [29–32], theoretical studies have been currently performed more than ever to elucidate neutron star physics through the nuclear EoS for dense matter. It has been found that the nuclear EoS should satisfy at least $2M_{\odot}$ to support the high-mass PSR J0740+6620 event, and that the precise measurements of neutron-star radii provide the valuable information in determining the features of isospin-asymmetric nuclear matter. In addition, the direct detection of gravitational-wave (GW) signals from a binary neutron star merger, GW170817, observed by Advanced LIGO and Advanced Virgo detectors has placed stringent restrictions on the mass–radius relation of neutron stars [33–35]. In particular, the tidal deformability of a neutron star [36, 37] plays a critical role in constructing the EoS for neutron star matter [38–41]. It has been reported that there are the strong correlations of neutron-star radii with $E_{\rm sym}$ and L, and the radius of a typical neutron star is determined by L [42–45]. Using a Bayesian analysis based on constraints from NICER and GW170817 within chiral effective field theory calculations, L is currently estimated as L = (43.7–70.0) MeV [46].

The accurate measurement of neutron skin thickness of ^{208}Pb, $R^{208}_{\rm skin}$, by the PREX Collaboration, using the parity-violating electron scattering, has revealed a serious discrepancy between the measured $R^{208}_{\rm skin}$ and theoretical predictions [47]. The neutron skin thickness, $R_{\rm skin}$, is defined here as the difference between the root-mean-square radii of point neutrons and protons, R_n and R_p, in a nucleus:

$$R_{\rm skin} = R_n - R_p. \tag{1}$$

To explain the PREX-2 result, Reed et al. [48] have proposed the large L value as $L = 106 \pm 37$ MeV, by exploiting the strong correlation between $R^{208}_{\rm skin}$ and L. In contrast, Reinhard et al. [49], using modern relativistic and non-relativistic energy density functionals, have predicted the smaller value, $L = 54 \pm 8$ MeV, by carefully assessing theoretical uncertainty on the parity-violating asymmetry, $A_{\rm PV}$, in ^{208}Pb. Additionally, the CREX experiment, which provides a precise measurement of the neutron skin thickness of ^{48}Ca, $R^{48}_{\rm skin}$, through the parity-violating electron scattering [50], complicates the understanding of isospin-asymmetric nuclear matter. This complexity arises from the difficulty of reconciling the PREX-2 and CREX results simultaneously. In addition, the measurements from polarized proton scattering off ^{208}Pb indicate smaller $R^{208}_{\rm skin}$, and consequently smaller L, compared to those obtained from the PREX-2 experiment [51, 52]. As a result, $R^{208}_{\rm skin}$ and L remain uncertain in theoretical calculations [53, 54]. At present, many species of neutron skin thickness have been reported from a combination of experimental and theoretical results [55].

In this article, we review the recently updated RMF models with non-linear couplings by introducing the isoscalar- and isovector-meson mixing, $\sigma^2\boldsymbol{\delta}^2$ and $\omega_\mu\omega^\mu\boldsymbol{\rho}_\nu\boldsymbol{\rho}^\nu$, which can cover both data from stable nuclear ground states and astrophysical observations of neutron stars. Although the isovector, Lorentz-scalar ($\boldsymbol{\delta}$) meson has been claimed to be less important than the isovector, Lorentz-vector ($\boldsymbol{\rho}^\mu$) meson so far, it has been recently realized that the δ meson considerably affects the properties of isospin-asymmetric nuclear EoS, such as neutron skin thickness of heavy nuclei and neutron-star radii [56–59] The new effective interactions discussed in this review are constructed under the constraints from the terrestrial experiments and astrophysical observations of neutron stars, especially focusing on the PREX-2 and CREX experiments. The resulting nuclear EoS have to support the following conditions:

(1) The EoSs for symmetric nuclear matter and pure neutron matter satisfy the particle flow data in heavy-ion collisions (HICs) [60–63],
(2) The EoS for neutron stars attains to the observed mass of PSR J0740+6620 $M = 2.072^{+0.067}_{-0.066}\,M_{\odot}$ [32, 64, 65],
(3) The EoS for neutron stars explains the dimensionless tidal deformability from the binary merger event, GW170817 ($\Lambda_{1.4} = 190^{+390}_{-120}$) [34, 35].

Under these constraints, we examine the effects of the δ-nucleon coupling and σ–δ mixing on the ground-state properties of finite nuclei, and consider the PREX-2 and CREX results. Additionally, we investigate the impact of the quartic self-interactions of δ and ρ mesons on the nuclear EoS to study the properties of neutron star matter.

This paper is organized as follows. A summary and analytical calculations concerning the RMF model with non-linear couplings are described in Section 2. Numerical results and detailed discussions are presented in Section 3. Finally, we give a summary in Section 4.

2 Theoretical framework

2.1 Lagrangian density

In quantum hydrodynamics [7], we employ the recently updated effective Lagrangian density including the isoscalar (σ and ω^μ) and isovector ($\boldsymbol{\delta}$ and $\boldsymbol{\rho}^\mu$) mesons as well as nucleons ($N = p, n$) [57, 58]. The total Lagrangian density is then given by

$$L = \bar{\psi}_N\left[i\gamma_\mu\partial^\mu - (M_N - g_\sigma\sigma - g_\delta\boldsymbol{\delta}\cdot\boldsymbol{\tau}_N) - g_\omega\gamma_\mu\omega^\mu - g_\rho\gamma_\mu\boldsymbol{\rho}^\mu\cdot\boldsymbol{\tau}_N\right]\psi_N + \frac{1}{2}\left(\partial_\mu\sigma\partial^\mu\sigma - m_\sigma^2\sigma^2\right) + \frac{1}{2}m_\omega^2\omega_\mu\omega^\mu - \frac{1}{4}W_{\mu\nu}W^{\mu\nu} + \frac{1}{2}\left(\partial_\mu\boldsymbol{\delta}\cdot\partial^\mu\boldsymbol{\delta} - m_\delta^2\boldsymbol{\delta}\cdot\boldsymbol{\delta}\right) + \frac{1}{2}m_\rho^2\boldsymbol{\rho}_\mu\cdot\boldsymbol{\rho}^\mu - \frac{1}{4}\boldsymbol{R}_{\mu\nu}\cdot\boldsymbol{R}^{\mu\nu} + L_{\rm EM} - U_{\rm NL}(\sigma,\omega,\boldsymbol{\delta},\boldsymbol{\rho}), \quad (2)$$

where $\psi_N = \begin{pmatrix}\psi_p\\ \psi_n\end{pmatrix}$ is the iso-doublet, nucleon field, $\boldsymbol{\tau}_N$ is its isospin matrix, $W_{\mu\nu} = \partial_\mu\omega_\nu - \partial_\nu\omega_\mu$, and $\boldsymbol{R}_{\mu\nu} = \partial_\mu\boldsymbol{\rho}_\nu - \partial_\nu\boldsymbol{\rho}_\mu$. The meson-nucleon coupling constants are respectively denoted by g_σ, g_ω, g_δ, and g_ρ. The photon-N interaction, $L_{\rm EM} = -e\bar{\psi}_p\gamma_\mu A^\mu\psi_p - \frac{1}{4}F_{\mu\nu}F^{\mu\nu}$ with $F_{\mu\nu} = \partial_\mu A_\nu - \partial_\nu A_\mu$, is also taken into account to describe the characteristics of finite nuclei [7, 66]. Additionally, a non-linear potential in Equation 1 is supplemented as follows:

$$U_{\rm NL}(\sigma,\omega,\boldsymbol{\delta},\boldsymbol{\rho}) = \frac{1}{3}g_2\sigma^3 + \frac{1}{4}g_3\sigma^4 - \frac{1}{4}c_3\left(\omega_\mu\omega^\mu\right)^2 + \frac{1}{4}d_3(\boldsymbol{\delta}\cdot\boldsymbol{\delta})^2 - \frac{1}{4}e_3\left(\boldsymbol{\rho}_\mu\cdot\boldsymbol{\rho}^\mu\right)^2 - \Gamma_{\sigma\delta}\sigma(\boldsymbol{\delta}\cdot\boldsymbol{\delta}) - \Lambda_{\sigma\delta}\sigma^2(\boldsymbol{\delta}\cdot\boldsymbol{\delta}) - \Lambda_{\omega\rho}\left(\omega_\mu\omega^\mu\right)\left(\boldsymbol{\rho}_\nu\cdot\boldsymbol{\rho}^\nu\right). \quad (3)$$

The first and second terms in Equation 2 are introduced to obtain a quantitative description of ground-state properties for symmetric nuclear matter [8, 67]. The quartic self-interactions of ω, δ, and ρ mesons are also introduced in Equation 2 [9, 10, 68, 69]. We also consider the isoscalar- and isovector-meson mixing, which only affects the characteristics of $N \neq Z$ finite nuclei and isospin-asymmetric nuclear matter [56, 70, 71], while the scalar-vector mixing is not included in the present study [11, 72–75].

2.2 Field equations for finite nuclei in mean-field approximation

In mean-field approximation, the meson and photon fields are replaced by the mean-field values: $\bar{\sigma}$, $\bar{\omega}$, $\bar{\delta}$, $\bar{\rho}$, and $\bar{A}$. Then, the effective nucleon mass in matter is simply expressed as

$$M^*_{N=\binom{p}{n}}(\bar{\sigma},\bar{\delta}) = M_N - g_\sigma\bar{\sigma} \mp g_\delta\bar{\delta}, \quad (4)$$

where M_N (= 939 MeV) is the nucleon mass in free space. If we restrict consideration to spherical finite nuclei, the equation of motion for N is given by

$$\left[-i\boldsymbol{\alpha}\cdot\boldsymbol{\nabla} + \beta M^*_{\binom{p}{n}}(\bar{\sigma},\bar{\delta}) + g_\omega\bar{\omega} \pm g_\rho\bar{\rho} + e\frac{1\pm1}{2}\bar{A}\right]\psi_{\binom{p}{n}} = E_{\alpha\binom{p}{n}}\psi_{\binom{p}{n}}, \quad (5)$$

with $E_{\alpha N}$ being the nucleon single-particle energy. The meson and photon fields are then given by

$$\left[-\boldsymbol{\nabla}^2 + m_\sigma^{*2}(\bar{\sigma},\bar{\delta})\right]\bar{\sigma} = g_\sigma\left(\rho_p^s + \rho_n^s\right), \quad (6)$$

$$\left[-\boldsymbol{\nabla}^2 + m_\omega^{*2}(\bar{\omega},\bar{\rho})\right]\bar{\omega} = g_\omega\left(\rho_p + \rho_n\right), \quad (7)$$

$$\left[-\boldsymbol{\nabla}^2 + m_\delta^{*2}(\bar{\sigma},\bar{\delta})\right]\bar{\delta} = g_\delta\left(\rho_p^s - \rho_n^s\right), \quad (8)$$

$$\left[-\boldsymbol{\nabla}^2 + m_\rho^{*2}(\bar{\omega},\bar{\rho})\right]\bar{\rho} = g_\rho\left(\rho_p - \rho_n\right), \quad (9)$$

and

$$-\boldsymbol{\nabla}^2\bar{A} = e\rho_p, \quad (10)$$

where ρ_N^s (ρ_N) is the scalar (baryon) density for N, which is computed self-consistently using nucleon wave functions in Equation 4 that are solutions to the Dirac equation in the spatially dependent meson and photon fields. The effective meson masses are defined by

$$m_\sigma^{*2}(\bar{\sigma},\bar{\delta}) = m_\sigma^2 + g_2\bar{\sigma} + g_3\bar{\sigma}^2 - \Gamma_{\sigma\delta}\bar{\delta}^2/\bar{\sigma} - 2\Lambda_{\sigma\delta}\bar{\delta}^2, \quad (11)$$

$$m_\omega^{*2}(\bar{\omega},\bar{\rho}) = m_\omega^2 + c_3\bar{\omega}^2 + 2\Lambda_{\omega\rho}\bar{\rho}^2, \quad (12)$$

$$m_\delta^{*2}(\bar{\sigma},\bar{\delta}) = m_\delta^2 + d_3\bar{\delta}^2 - 2\Gamma_{\sigma\delta}\bar{\sigma} - 2\Lambda_{\sigma\delta}\bar{\sigma}^2, \quad (13)$$

$$m_\rho^{*2}(\bar{\omega},\bar{\rho}) = m_\rho^2 + e_3\bar{\rho}^2 + 2\Lambda_{\omega\rho}\bar{\omega}^2. \quad (14)$$

The total energy of the system is thus written as

$$E_{\rm tot} = \sum_{N=p,n}\sum_\alpha^{\rm occ}(2j_\alpha+1)E_{\alpha N} + \frac{1}{2}\int d\boldsymbol{r}\left[g_\sigma\left(\rho_p^s + \rho_n^s\right)\bar{\sigma} - g_\omega\left(\rho_p + \rho_n\right)\bar{\omega} + g_\delta\left(\rho_p^s - \rho_n^s\right)\bar{\delta} - g_\rho\left(\rho_p - \rho_n\right)\bar{\rho} - e\rho_p\bar{A} + \frac{1}{2}\int d\boldsymbol{r}\left(-\frac{1}{3}g_2\bar{\sigma}^3 - \frac{1}{2}g_3\bar{\sigma}^4 + \frac{1}{2}c_3\bar{\omega}^4 - \frac{1}{2}d_3\bar{\delta}^4 + \frac{1}{2}e_3\bar{\rho}^4 + \Gamma_{\sigma\delta}\bar{\sigma}\bar{\delta}^2 + 2\Lambda_{\sigma\delta}\bar{\sigma}^2\bar{\delta}^2 + 2\Lambda_{\omega\rho}\bar{\omega}^2\bar{\rho}^2\right)\right], \quad (15)$$

where the sum α runs over the occupied states of $E_{\alpha N}$ with the degeneracy $(2j_\alpha+1)$ [7].

2.3 Infinite nuclear matter

To study the bulk properties of nuclear and neutron star matter, it is necessary to compute the nuclear equation of state (EoS)—a relation between the energy density, ε_B, and pressure, P_B. In infinite nuclear matter, the surface terms in Equations 5–9 have no influence on its characteristics as the gradient reads zero. The scalar and baryon density for N (= p,n) are then obtained as

$$\rho_N^s = \langle\bar{\psi}_N\psi_N\rangle = \frac{1}{\pi^2}\int_0^{k_{F_N}}dkk^2\frac{M_N^*}{\sqrt{k^2+M_N^{*2}}} = \frac{M_N^{*3}}{2\pi^2}\left[\frac{k_{F_N}E_N^*}{M_N^{*2}} - \ln\left(\frac{k_{F_N}+E_N^*}{M_N^*}\right)\right], \quad (16)$$

$$\rho_N = \langle\psi_N^\dagger\psi_N\rangle = \frac{1}{\pi^2}\int_0^{k_{F_N}}dkk^2 = \frac{k_{F_N}^3}{3\pi^2}, \quad (17)$$

where k_{F_N} and $E_N^*\left(=\sqrt{k_{F_N}^2+M_N^{*2}}\right)$ are the Fermi momentum and energy for N. With the self-consistent calculations of the meson fields, ε_B and P_B are respectively given by $\varepsilon_B = \sum_N\varepsilon_N + \varepsilon_M$ and $P_B = \sum_N P_N + P_M$ where the nucleon and meson parts are expressed as

$$\varepsilon_N = \frac{1}{\pi^2}\int_0^{k_{F_N}}dkk^2\sqrt{k^2+M_N^{*2}} = \frac{1}{4}\left(3E_N^*\rho_N + M_N^*\rho_N^s\right), \quad (18)$$

$$P_N = \frac{1}{3\pi^2}\int_0^{k_{F_N}}dk\frac{k^4}{\sqrt{k^2+M_N^{*2}}} = \frac{1}{4}\left(E_N^*\rho_N - M_N^*\rho_N^s\right), \quad (19)$$

and

$$\varepsilon_M = \frac{1}{2}\left(m_\sigma^2\bar{\sigma}^2 + m_\omega^2\bar{\omega}^2 + m_\delta^2\bar{\delta}^2 + m_\rho^2\bar{\rho}^2\right) + \frac{1}{3}g_2\bar{\sigma}^3 + \frac{1}{4}g_3\bar{\sigma}^4 + \frac{3}{4}c_3\bar{\omega}^4 + \frac{1}{4}\bar{\delta}^4 + \frac{3}{4}e_3\bar{\rho}^4 - \Gamma_{\sigma\delta}\bar{\sigma}\bar{\delta}^2 - \Lambda_{\sigma\delta}\bar{\sigma}^2\bar{\delta}^2 + 3\Lambda_{\omega\rho}\bar{\omega}^2\bar{\rho}^2, \quad (20)$$

$$P_M = -\frac{1}{2}\left(m_\sigma^2\bar{\sigma}^2 - m_\omega^2\bar{\omega}^2 + m_\delta^2\bar{\delta}^2 - m_\rho^2\bar{\rho}^2\right) - \frac{1}{3}g_2\bar{\sigma}^3 - \frac{1}{4}g_3\bar{\sigma}^4 + \frac{1}{4}c_3\bar{\omega}^4 - \frac{1}{4}\bar{\delta}^4 + \frac{1}{4}e_3\bar{\rho}^4 + \Gamma_{\sigma\delta}\bar{\sigma}\bar{\delta}^2 + \Lambda_{\sigma\delta}\bar{\sigma}^2\bar{\delta}^2 + \Lambda_{\omega\rho}\bar{\omega}^2\bar{\rho}^2. \quad (21)$$

2.4 Nuclear bulk properties

In general, the bulk properties of infinite nuclear matter are identified by the expansion of isospin-asymmetric nuclear EoS with a power series in the isospin asymmetry, $\alpha = (\rho_n - \rho_p)/\rho_B$, and the total baryon density, $\rho_B\left(=\rho_n+\rho_p\right)$ [76, 77]. The binding energy per nucleon is then written as

$$E_B(\rho_B,\alpha) = \frac{\varepsilon_B(\rho_B,\alpha)}{\rho_B} - M_N = E_0(\rho_B) + E_{\rm sym}(\rho_B)\alpha^2 + O(\alpha^4), \quad (22)$$

where $E_0(\rho_B)$ is the binding energy per nucleon of symmetric nuclear matter (SNM) and $E_{\rm sym}(\rho_B)$ is the nuclear symmetry energy (NSE),

$$E_{\rm sym}(\rho_B) = \frac{1}{2}\left.\frac{\partial^2 E_B(\rho_B,\alpha)}{\partial\alpha^2}\right|_{\alpha=0}. \quad (23)$$

Besides, $E_0(\rho_B)$ and $E_{\rm sym}(\rho_B)$ can be expanded around the nuclear saturation density, ρ_0, as

$$E_0(\rho_B) = E_0(\rho_0) + \frac{K_0}{2}\chi^2 + \frac{J_0}{6}\chi^3 + O(\chi^4), \quad (24)$$

$$E_{\rm sym}(\rho_B) = E_{\rm sym}(\rho_0) + L\chi + \frac{K_{\rm sym}}{2}\chi^2 + \frac{J_{\rm sym}}{6}\chi^3 + O(\chi^4), \quad (25)$$

with $\chi = (\rho_B - \rho_0)/3\rho_0$ being the dimensionless variable characterizing the deviations of ρ_B from ρ_0. The incompressibility coefficient of SNM, K_0, the slope and curvature parameters of NSE, L and $K_{\rm sym}$, and the third-order incompressibility coefficients of SNM and NSE, J_0 and $J_{\rm sym}$, are respectively defined as

$$K_0 = 9\rho_B^2\left.\frac{d^2E_0(\rho_B)}{d\rho_B^2}\right|_{\rho_B=\rho_0}, \quad (26)$$

$$L = 3\rho_B\left.\frac{dE_{\rm sym}(\rho_B)}{d\rho_B}\right|_{\rho_B=\rho_0}, \quad K_{\rm sym} = 9\rho_B^2\left.\frac{d^2E_{\rm sym}(\rho_B)}{d\rho_B^2}\right|_{\rho_B=\rho_0}, \quad (27)$$

$$J_0 = 27\rho_B^3\left.\frac{d^3E_0(\rho_B)}{d\rho_B^3}\right|_{\rho_B=\rho_0}, \quad J_{\rm sym} = 27\rho_B^3\left.\frac{d^3E_{\rm sym}(\rho_B)}{d\rho_B^3}\right|_{\rho_B=\rho_0}. \quad (28)$$

Taking into account the thermodynamic condition, the pressure of infinite nuclear matter, $P_B(\rho_B,\alpha)$, is given by

$$P_B(\rho_B,\alpha) = \rho_B^2\frac{\partial E_B(\rho_B,\alpha)}{\partial\rho_B} = \rho_B^2\frac{\partial}{\partial\rho_B}\left[\frac{\varepsilon_B(\rho_B,\alpha)}{\rho_B} - M_N\right] = \rho_B\frac{\partial\varepsilon_B(\rho_B,\alpha)}{\partial\rho_B} - \varepsilon_B(\rho_B,\alpha), \quad (29)$$

with the binding energy per nucleon in Equation 14. The nuclear incompressibility, $K_B(\rho_B,\alpha)$, is then expressed as

$$K_B(\rho_B,\alpha) = 9\rho_B^2\frac{\partial^2E_B(\rho_B,\alpha)}{\partial\rho_B^2} = 9\rho_B^2\frac{\partial}{\partial\rho_B}\left[\frac{P_B(\rho_B,\alpha)}{\rho_B^2}\right] = 9\left[\frac{\partial P_B(\rho_B,\alpha)}{\partial\rho_B} - 2\frac{P_B(\rho_B,\alpha)}{\rho_B}\right]. \quad (30)$$

Hence, the incompressibility coefficient of SNM, K_0, in Equation 16 is related with K_B through $K_0 = K_B(\rho_0,0)$. In the RMF calculation, we can obtain the analytical expression of $K_B(\rho_B,\alpha)$ using the following equation:

$$\frac{\partial P_B}{\partial\rho_B} = \frac{1}{3\rho_B}\sum_{N=p,n}\rho_N\frac{k_{F_N}^2}{E_N^*} - \sum_{N=p,n}\rho_N\frac{M_N^*}{E_N^*}\left[g_\sigma\frac{\partial\bar{\sigma}}{\partial\rho_B} + g_\delta(\boldsymbol{\tau}_N)_3\frac{\partial\bar{\delta}}{\partial\rho_B}\right] + m_\omega^{*2}\bar{\omega}\frac{\partial\bar{\omega}}{\partial\rho_B} + m_\rho^{*2}\bar{\rho}\frac{\partial\bar{\rho}}{\partial\rho_B}, \quad (31)$$

where the density derivatives of meson fields are calculated through the relation

$$\frac{\partial M}{\partial\rho_B} = \sum_{N=p,n}\frac{\rho_N}{\rho_B}\frac{\partial M}{\partial\rho_N} \quad (M=\bar{\sigma},\bar{\omega},\bar{\delta},\bar{\rho}), \quad (32)$$

with

$$\frac{\partial\bar{\sigma}}{\partial\rho_N} = \frac{M_N^*}{E_N^*}\frac{G_\sigma + G_\delta(\boldsymbol{\tau}_N)_3H_{\sigma\delta}}{1 - H_{\sigma\delta}H_{\delta\sigma}}, \quad \frac{\partial\bar{\omega}}{\partial\rho_N} = \frac{G_\omega - G_\rho(\boldsymbol{\tau}_N)_3H_{\omega\rho}}{1 - H_{\omega\rho}H_{\rho\omega}}, \quad (33)$$

$$\frac{\partial\bar{\delta}}{\partial\rho_N} = \frac{M_N^*}{E_N^*}\frac{G_\sigma H_{\delta\sigma} + G_\delta(\boldsymbol{\tau}_N)_3}{1 - H_{\sigma\delta}H_{\delta\sigma}}, \quad \frac{\partial\bar{\rho}}{\partial\rho_N} = \frac{-G_\omega H_{\rho\omega} + G_\rho(\boldsymbol{\tau}_N)_3}{1 - H_{\omega\rho}H_{\rho\omega}}, \quad (34)$$

and

$$(\boldsymbol{\tau}_N)_3 = \begin{cases} +1 \\ -1 \end{cases} \quad \text{for } N = \begin{pmatrix} p \\ n \end{pmatrix}. \quad (35)$$

We here use the following quantities:

$$G_\sigma = \frac{g_\sigma}{M_\sigma^2}, \quad G_\omega = \frac{g_\omega}{M_\omega^2}, \quad G_\delta = \frac{g_\delta}{M_\delta^2}, \quad G_\rho = \frac{g_\rho}{M_\rho^2}, \quad (36)$$

and

$$H_{\sigma\delta} = \frac{L_{\sigma\delta}^2}{M_\sigma^2}, \quad H_{\delta\sigma} = \frac{L_{\sigma\delta}^2}{M_\delta^2}, \quad H_{\omega\rho} = \frac{4\Lambda_{\omega\rho}\bar{\omega}\bar{\rho}}{M_\omega^2}, \quad H_{\rho\omega} = \frac{4\Lambda_{\omega\rho}\bar{\omega}\bar{\rho}}{M_\rho^2}, \quad (37)$$

with

$$M_\sigma^2(\bar{\sigma},\bar{\delta}) = m_\sigma^{*2}(\bar{\sigma},\bar{\delta}) + g_2\bar{\sigma} + 2g_3\bar{\sigma}^2 + \Gamma_{\sigma\delta}\bar{\delta}^2/\bar{\sigma} + g_\sigma^2\left(J_p + J_n\right), \quad (38)$$

$$M_\omega^2(\bar{\omega},\bar{\rho}) = m_\omega^{*2}(\bar{\omega},\bar{\rho}) + 2c_3\bar{\omega}^2, \quad (39)$$

$$M_\delta^2(\bar{\sigma},\bar{\delta}) = m_\delta^{*2}(\bar{\sigma},\bar{\delta}) + 2d_3\bar{\delta}^2 + g_\delta^2\left(J_p + J_n\right), \quad (40)$$

$$M_\rho^2(\bar{\omega},\bar{\rho}) = m_\rho^{*2}(\bar{\omega},\bar{\rho}) + 2e_3\bar{\rho}^2, \quad (41)$$

$$L_{\sigma\delta}^2(\bar{\sigma},\bar{\delta}) = 2\Gamma_{\sigma\delta}\bar{\delta} + 4\Lambda_{\sigma\delta}\bar{\sigma}\bar{\delta} - g_\sigma g_\delta\left(J_p - J_n\right), \quad (42)$$

where the effective meson masses, m_σ^{*2}, m_ω^{*2}, m_δ^{*2} and m_ρ^{*2}, are given in Equations 10–13, and J_N for $N\,(=p,n)$ reads

$$J_N = 3\left(\frac{\rho_N^s}{M_N^*} - \frac{\rho_N}{E_N^*}\right). \tag{43}$$

According to the Hugenholtz-Van Hove theorem in nuclear matter, $E_{\rm sym}$ defined in Equation 15 can be generally written as

$$\begin{aligned} E_{\rm sym}(\rho_B) &= \frac{1}{2}\frac{\partial}{\partial\alpha}\left[\frac{\partial E_B(\rho_B,\alpha)}{\partial\alpha}\right]_{\alpha=0} \\ &= \frac{1}{8}\rho_B\left(\frac{\partial}{\partial\rho_p} - \frac{\partial}{\partial\rho_n}\right)\left[E_p\left(k_{F_p}\right) - E_n\left(k_{F_n}\right)\right]\Big|_{\rho_p=\rho_n}, \end{aligned} \tag{44}$$

where E_N is the single-particle energy for N, which is determined self-consistently by solving the following transcendental equation [78, 79]:

$$E_N(k) = \left[E_N^*(k) - \sum_N^0(k)\right]_{k^0=E_N(k)}. \tag{45}$$

The effective mass, (four) momentum, and energy for N are here defined as [80, 81]

$$M_N^*(k) = M_N + \sum_N^s(k), \tag{46}$$

$$\begin{aligned} k_N^{\mu*} &= \left(k_N^{*0}, \boldsymbol{k}_N^*\right) \\ &= \left(k^0 + \sum_N^0(k), \boldsymbol{k} + \hat{k}\sum_N^v(k)\right), \end{aligned} \tag{47}$$

$$E_N^*(k) = \sqrt{\boldsymbol{k}_N^{*2} + M_N^{*2}(k)}, \tag{48}$$

with $\Sigma_N^{s(0)[v]}$ being the scalar (time) [space] component of nucleon self-energy. In addition, $E_{\rm sym}$ is divided into the kinetic and potential terms as

$$E_{\rm sym}(\rho_B) = E_{\rm sym}^{\rm kin}(\rho_B) + E_{\rm sym}^{\rm pot}(\rho_B). \tag{49}$$

Based on the Lorentz-covariant decomposition of NSE [82], $E_{\rm sym}^{\rm pot}$ is expressed as

$$E_{\rm sym}^{\rm pot}(\rho_B) = E_{\rm sym}^s(\rho_B) + E_{\rm sym}^0(\rho_B) + E_{\rm sym}^v(\rho_B), \tag{50}$$

with the scalar (s), time (0), and space (v) components. The $E_{\rm sym}$ is thus computed as follows:

$$E_{\rm sym}^{\rm kin}(\rho_B) = \frac{1}{6}\frac{k_F^*}{E_F^*}k_F, \tag{51}$$

$$E_{\rm sym}^s(\rho_B) = \frac{1}{8}\rho_B\frac{M_F^*}{E_F^*}\left(\frac{\partial}{\partial\rho_p} - \frac{\partial}{\partial\rho_n}\right)\left(\sum_p^s - \sum_n^s\right)\Big|_{\rho_p=\rho_n}, \tag{52}$$

$$E_{\rm sym}^0(\rho_B) = -\frac{1}{8}\rho_B\left(\frac{\partial}{\partial\rho_p} - \frac{\partial}{\partial\rho_n}\right)\left(\sum_p^0 - \sum_n^0\right)\Big|_{\rho_p=\rho_n}, \tag{53}$$

$$E_{\rm sym}^v(\rho_B) = \frac{1}{8}\rho_B\frac{k_F^*}{E_F^*}\left(\frac{\partial}{\partial\rho_p} - \frac{\partial}{\partial\rho_n}\right)\left(\sum_p^v - \sum_n^v\right)\Big|_{\rho_p=\rho_n}, \tag{54}$$

where the effective quantities at the Fermi surface in Equations 22–25 are then given by $M_F^* = M_p^*(k_F) = M_n^*(k_F)$, $k_F^* = |\boldsymbol{k}_p^*(k_F)| = |\boldsymbol{k}_n^*(k_F)|$, and $E_F^* = E_p^*(k_F) = E_n^*(k_F)$ at $\rho_p = \rho_n$, namely, $k_{F_p} = k_{F_n} = k_F$. In RMF approximation, $\Sigma_N^{s,0,v}$ are respectively given by

$$\sum_N^s = -g_\sigma\bar{\sigma} - g_\delta(\boldsymbol{\tau}_N)_3\bar{\delta}, \tag{55}$$

$$\sum_N^0 = -g_\omega\bar{\omega} - g_\rho(\boldsymbol{\tau}_N)_3\bar{\rho}, \tag{56}$$

$$\sum_N^v = 0. \tag{57}$$

Using Equations 20, 21, $E_{\rm sym}$ can be finally expressed as

$$\begin{aligned} E_{\rm sym}(\rho_B) &= E_{\rm sym}^{\rm kin}(\rho_B) + E_{\rm sym}^s(\rho_B) + E_{\rm sym}^0(\rho_B) \\ &= \frac{1}{6}\frac{k_F^2}{E_F^*} - \frac{1}{2}\frac{g_\delta^2}{M_\delta^2(\bar{\sigma},0)}\left(\frac{M_F^*}{E_F^*}\right)^2\rho_B + \frac{1}{2}\frac{g_\rho^2}{M_\rho^2(\bar{\omega},0)}\rho_B. \end{aligned} \tag{58}$$

Note that $k_F^* = k_F$ and $E_{\rm sym}^v(\rho_B) = 0$ in RMF approximation. The L and $K_{\rm sym}$ given in Equation 17 are also expressed as

$$\begin{aligned} L &= L^{\rm kin} + L^{\rm pot} \\ &= L^{\rm kin} + L^s + L^0, \end{aligned} \tag{59}$$

$$\begin{aligned} K_{\rm sym} &= K_{\rm sym}^{\rm kin} + K_{\rm sym}^{\rm pot} \\ &= K_{\rm sym}^{\rm kin} + K_{\rm sym}^s + K_{\rm sym}^0, \end{aligned} \tag{60}$$

where the kinetic, scalar, and time components are respectively given by

$$L^{\rm kin} = E_{\rm sym}^{\rm kin}(\rho_0)\left[1 + \left(\frac{M_F^*}{E_F^*}\right)^2 K_B(\rho_0)\right], \tag{61}$$

$$L^{s(0)} = 3E_{\rm sym}^{s(0)}(\rho_0)\left[1 - \rho_0 T_B^{s(0)}(\rho_0)\right], \tag{62}$$

$$K_{\rm sym}^{\rm kin} = -2L^{\rm kin} + \left(\frac{M_F^*}{E_F^*}\right)^2\left[E_{\rm sym}^{\rm kin}(\rho_0)N_B(\rho_0) + L^{\rm kin}K_B(\rho_0)\right], \tag{63}$$

$$K_{\rm sym}^{s(0)} = 3L^{s(0)}\left[1 - \rho_0 T_B^{s(0)}(\rho_0)\right] - 9E_{\rm sym}^{s(0)}\left[1 + \rho_0^2\frac{dT_B^{s(0)}(\rho_B)}{d\rho_B}\Big|_{\rho_B=\rho_0}\right], \tag{64}$$

with

$$K_B(\rho_B) = 1 + 3\frac{g_\sigma^2}{M_\sigma^2(\bar{\sigma},0)}\frac{\rho_B}{E_F^*}, \tag{65}$$

$$\begin{aligned} T_B^s(\rho_B) &= \frac{2}{3\rho_B}\left(\frac{k_F}{E_F^*}\right)^2 K_B(\rho_B) - \frac{g_\sigma\left(2\Gamma_{\sigma\delta} + 4\Lambda_{\sigma\delta}\bar{\sigma}\right)}{M_\sigma^2(\bar{\sigma},0)M_\delta^2(\bar{\sigma},0)}\frac{M_F^*}{E_F^*} \\ &\quad + \frac{g_\delta^2}{M_\delta^2(\bar{\sigma},0)}\left[\left(\frac{k_F}{E_F^*}\right)^2\frac{K_B(\rho_B)}{E_F^*} - 2\frac{g_\sigma^2}{M_\sigma^2(\bar{\sigma},0)}\frac{J_p + J_n}{E_F^*}\right], \end{aligned} \tag{66}$$

$$T_B^0(\rho_B) = \frac{4g_\omega\Lambda_{\omega\rho}\bar{\omega}}{M_\omega^2(\bar{\omega},0)M_\rho^2(\bar{\omega},0)}, \tag{67}$$

$$N_B(\rho_B) = 3\rho_B\frac{dK_B(\rho_B)}{d\rho_B} - 2\left(\frac{k_F}{E_F^*}\right)^2 K_B^2(\rho_B). \tag{68}$$

2.5 Stability of nuclear and neutron star matter

In order to move on the calculations of neutron stars in which the charge neutrality and β equilibrium conditions are imposed, we

introduce the degrees of freedom of leptons (electrons and muons) as well as nucleons and mesons in Equation 2.

$$L_L = \bar{\psi}_\ell \left(i\gamma_\mu \partial^\mu - \widehat{m}_\ell \right) \psi_\ell, \tag{69}$$

where $\psi_\ell = \begin{pmatrix} \psi_e \\ \psi_\mu \end{pmatrix}$ is the lepton field and its mass is given by $\widehat{m}_\ell = \mathrm{diag}(m_e, m_\mu)$.

When we consider the stability of matter in cold neutron stars, the first principle of thermodynamics should be considered:

$$du = -Pdv - \mu dq, \tag{70}$$

with u, P, $v\,(=1/\rho_B)$, μ, and q being the total internal energy per nucleon, pressure, volume per nucleon, chemical potential, and charge fraction, respectively [83–86]. In neutron star matter, the charge neutrality and β equilibrium conditions read

$$\mu = \mu_n - \mu_p = \mu_e = \mu_\mu, \tag{71}$$

$$q = Y_p - Y_L = \rho_p/\rho_B - \sum_{\ell=e,\mu} \rho_\ell/\rho_B = 0, \tag{72}$$

with ρ_ℓ the lepton density. The stability of neutron star matter are then expressed as the following two constraints on chemical potential and pressure:

$$-\left(\frac{\partial \mu}{\partial q}\right)_v > 0, \tag{73}$$

$$-\left(\frac{\partial P}{\partial v}\right)_\mu > 0. \tag{74}$$

The total internal energy per baryon, $u(v,q)$, can be decomposed into the baryon (B) and lepton (L) contributions as

$$u(v,q) = u(\rho_B,\alpha) = E_B(\rho_B,\alpha) + E_L(\rho_B,\alpha), \tag{75}$$

with $\alpha = 1 - 2Y_p$. At zero temperature, the β equilibrium condition leads to the relation [87].

$$\begin{aligned} \mu &= -\left(\frac{\partial E_B}{\partial Y_p}\right)_{\rho_B} \\ &= 2\left(\frac{\partial E_B}{\partial \alpha}\right)_{\rho_B} = 2E_{\mathrm{ISB}}(\rho_B,\alpha). \end{aligned} \tag{76}$$

where the isospin symmetry breaking (ISB) energy of infinite nuclear matter is given by

$$\begin{aligned} E_{\mathrm{ISB}}(\rho_B,\alpha) &= \left[\frac{\partial E_B(\rho_B,\alpha)}{\partial \alpha}\right]_{\rho_B} \\ &= \frac{1}{2}\left[E_n\left(k_{F_n}\right) - E_p\left(k_{F_p}\right)\right]. \end{aligned} \tag{77}$$

Considering the differentiation of $\mu(v,q)\,(=\mu(\rho_B,\alpha))$, we find

$$\begin{aligned} -\left(\frac{\partial q}{\partial \mu}\right)_v &= \frac{1}{2}\left(\frac{\partial \alpha}{\partial \mu}\right)_{\rho_B} + \frac{1}{\rho_B}\sum_{\ell=e,\mu}\left(\frac{\partial \rho_\ell}{\partial \mu}\right)_{\rho_B} \\ &= \frac{1}{8E_{\mathrm{sym}}(\rho_B,\alpha)} + \frac{\mu}{\pi^2\rho_B}\left(k_{F_e} + k_{F_\mu}\right) =: V_\mu(\rho_B,\alpha), \end{aligned} \tag{78}$$

where k_{F_e} and k_{F_μ} are respectively the Fermi momenta for electrons (e) and muons (μ). For simplicity, we here define the nuclear symmetry energy involving the isospin asymmetry, α, as

$$\begin{aligned} E_{\mathrm{sym}}(\rho_B,\alpha) &= \frac{1}{2}\frac{\partial^2 E_B(\rho_B,\alpha)}{\partial \alpha^2} \\ &= \frac{1}{2}\frac{\partial E_{\mathrm{ISB}}(\rho_B,\alpha)}{\partial \alpha}. \end{aligned} \tag{79}$$

Note that we explicitly keep α to consider the stability of nuclear and neutron star matter, though the nuclear symmetry energy is in general calculated at $\rho_p = \rho_n$, namely, $\alpha = 0$, as shown in Equation 15. Hence the stability constraint on chemical potential, $V_\mu(\rho_B,\alpha) > 0$, can be satisfied by assuming that $E_{\mathrm{sym}}(\rho_B,\alpha)$ is positive at any ρ_B.

As for the pressure stability, the differentiation of $P(v,q)\,(=P(\rho_B,\alpha))$ reads

$$-\left(\frac{\partial P}{\partial v}\right)_\mu = \rho_B^2\left[\left(\frac{\partial P_B}{\partial \rho_B}\right)_\mu + \left(\frac{\partial P_L}{\partial \rho_B}\right)_\mu\right], \tag{80}$$

with the baryon and lepton contributions. Similar to Equation 27, the baryon contribution is given by

$$\begin{aligned} \left(\frac{\partial P_B}{\partial \rho_B}\right)_\mu &= 2\rho_B\frac{\partial E_B(\rho_B,\alpha)}{\partial \rho_B} + \rho_B^2\frac{\partial^2 E_B(\rho_B,\alpha)}{\partial^2 \rho_B} \\ &\quad - \rho_B^2\left[\frac{\partial^2 E_B(\rho_B,\alpha)}{\partial \rho_B \partial \alpha}\right]^2 \Bigg/ \frac{\partial^2 E_B(\rho_B,\alpha)}{\partial^2 \alpha}. \end{aligned} \tag{81}$$

Using the thermodynamic definitions of pressure and incompressibility of infinite nuclear matter in Equations 18, 19, this equation can be simplified as

$$\left(\frac{\partial P_B}{\partial \rho_B}\right)_\mu = 2\frac{P_B(\rho_B,\alpha)}{\rho_B} + \frac{1}{9}K_B(\rho_B,\alpha) - \frac{1}{18}\frac{L_{\mathrm{ISB}}^2(\rho_B,\alpha)}{E_{\mathrm{sym}}(\rho_B,\alpha)}, \tag{82}$$

where the slope of ISB energy, $L_{\mathrm{ISB}}(\rho_B,\alpha)$, is defined as

$$L_{\mathrm{ISB}}(\rho_B,\alpha) = 3\rho_B\frac{\partial E_{\mathrm{ISB}}(\rho_B,\alpha)}{\partial \rho_B}. \tag{83}$$

The lepton contribution is also given by the simple form under the β equilibrium condition:

$$\left(\frac{\partial P_L}{\partial \rho_B}\right)_\mu = \frac{\rho_e k_{F_e}^2 + \rho_\mu k_{F_\mu}^2}{3\mu\rho_B}. \tag{84}$$

Therefore, the stability of neutron star matter under the charge neutrality and β equilibrium conditions can be clarified by the thermodynamic constraints on chemical potential and pressure, namely, $V_\mu(\rho_B,\alpha) > 0$ and

$$V_P(\rho_B,\alpha) := \left(\frac{\partial P_B}{\partial \rho_B}\right)_\mu + \left(\frac{\partial P_L}{\partial \rho_B}\right)_\mu > 0. \tag{85}$$

The thermodynamic stability is used in several calculations of nuclear and neutron star matter, for instance, the compressibility of β-equilibrated matter [56, 88] and the phase transition between the crust and core regions in neutron stars [89–91].

3 Results and discussions

3.1 Nuclear models

We adopt the recently developed effective interactions labeled as the OMEG family, which are constructed to reproduce the characteristics of finite nuclei, nuclear matter, and neutron stars [58, 92]. In particular, the δ–N coupling and σ–δ mixing in the

TABLE 1 Model parameters for various effective interactions.

Models	m_σ (MeV)	m_ω (MeV)	m_ρ (MeV)	g_σ^2	g_ω^2	g_δ^2	g_ρ^2	g_2 (fm^{-1})	g_3	c_3	$\Lambda_{\sigma\delta}$	$\Lambda_{\omega\rho}$
OMEG0	496.500	782.660	775.260	89.384	142.847	37.699	51.744	9.976	−21.469	—	87.000	102.612
OMEG1	497.825	782.660	775.260	99.645	166.268	30.000	44.591	7.824	−1.115	100.000	95.000	75.677
OMEG2	497.820	782.660	775.260	99.641	166.269	20.000	44.364	7.823	−1.113	100.000	85.000	288.859
OMEG3	498.015	782.660	775.260	99.713	166.272	15.000	57.550	7.827	−1.105	100.000	70.000	909.825
BigApple	492.730	782.500	763.000	93.507	151.684	—	50.139	11.944	−31.832	2.684	—	1449.033
DINOa	490.050	782.500	763.000	93.942	154.443	278.788	201.454	11.501	−20.139	59.626	—	205.236
DINOb	485.795	782.500	763.000	91.032	150.806	313.178	219.270	11.651	−20.561	56.870	—	185.311
DINOc	484.162	782.500	763.000	90.648	151.032	335.813	230.653	11.642	−20.517	57.039	—	171.604
FSU-δ6.2	491.500	782.500	763.000	104.332	180.507	38.440	48.867	8.090	5.881	172.150	107.650	91.639
FSU-δ6.7	491.500	782.500	763.000	104.332	180.507	44.890	52.843	8.090	5.881	172.150	90.157	102.004
FSUGarnet	496.939	782.500	763.000	110.350	187.693	—	47.966	9.565	−7.122	137.981	—	1555.729
FSUGarnet+R	495.633	782.500	763.000	109.045	186.307	—	35.654	9.407	−6.452	138.011	—	1016.385
FSUGold	491.500	782.500	763.000	112.204	204.556	—	34.629	4.277	49.858	418.394	—	850.374
FSUGold2	497.479	782.500	763.000	108.070	183.733	—	20.145	8.546	−1.021	144.122	—	12.289
FSUGold2+R	501.611	782.500	763.000	103.793	169.483	—	32.090	10.150	−19.026	55.970	—	687.024
HPNL0	501.825	782.500	770.000	109.108	180.637	1.443	26.967	9.393	−3.405	134.110	—	267.522
HPNL5	500.972	782.500	770.000	103.502	169.568	8.903	39.724	9.270	−2.866	120.751	46.077	511.487
IOPB-I	500.000	782.500	762.500	107.971	178.268	—	30.955	10.517	−15.146	91.108	—	528.819
IU-FSU	491.500	782.500	763.000	99.427	169.835	—	46.172	8.497	0.462	144.219	—	1442.856
NL3	508.194	782.501	763.000	104.408	165.562	—	19.883	10.454	−28.955	—	—	—
PD15	480.025	780.000	763.000	97.535	173.792	22.782	60.551	7.662	6.551	169.689	—	627.406
TAMUC-FSUa	502.200	782.500	763.000	106.504	176.178	—	24.339	8.830	−6.317	103.462	—	213.858
TM1	511.198	783.000	770.000	100.580	159.111	—	21.459	7.249	0.610	71.308	—	—

The nucleon and δ-meson masses in free space are fixed at $M_N = 939$ MeV and $m_\delta = 980$ MeV. For the HPNL0 and HPNL5, we set $m_\delta = 983$ MeV [101]. The M_N is taken as $M_N = 938$ MeV only for the TM1 [9].

OMEG family are determined so as to support the astrophysical constraints on the neutron-star radii from the NICER mission [29–32] and the tidal deformabilities from the binary merger events due to GW signals [34, 93]. Various theoretical calculations using the well-calibrated parameter sets based on the RMF models are also presented: BigApple [94], DINO [95], FSU-δ [59], FSUGarnet [96], FSUGold [97], FSUGold2 [98], Bayesian refinement of FSUGarnet and FSUGold2, FSUGarnet+R and FSUGold2+R [99, 100], HPNL0 and HPNL5 [101], IOPB-I [102], IU-FSU [103], NL3 [67], PD15 [104], TAMUC-FSUa [105, 106], and TM1 [9]. In Tables 1, 2, we summarize the model parameters and the properties of symmetric nuclear matter at ρ_0 for the effective interactions used in the present study.

In addition, we present the extended interactions based on the FSUGarnet, TAMUC-FSUa, and FSUGold2 models, in which the δ–N coupling are introduced to investigate the effect of δ meson. Since the δ–N coupling only influences the properties of $N \neq Z$ finite nuclei and isospin-asymmetric nuclear matter, we adjust g_ρ^2 and $\Lambda_{\omega\rho}$ to preserve the original model's predictions for L when the δ–N coupling is included. Simultaneously, the other

10.3389/fphy.2024.1531475

TABLE 2 Properties of symmetric nuclear matter at ρ_0 for various effective interactions.

Models	ρ_0	M_N^*/M_N	E_0	K_0	J_0	E_{sym}	L	K_{sym}	J_{sym}	K_{asy}	$K_{sat,2}$	K_N
	(fm^{-3})		(MeV)	(MeV)	(MeV)	(MeV)	(MeV)	(MeV)	(MeV)	(MeV)	(MeV)	(MeV)
OMEG0	0.1500	0.640	−16.45	280.00	−66.98	34.55	50.00	−384.43	−533.44	−684.43	−672.47	−104.43
OMEG1	0.1484	0.620	−16.38	256.00	−300.62	35.06	70.00	−218.83	−68.94	−638.83	−556.62	37.17
OMEG2	0.1484	0.620	−16.38	256.00	−300.56	33.00	45.00	−216.72	1020.63	−486.72	−433.89	39.28
OMEG3	0.1484	0.620	−16.38	256.00	−300.28	30.00	20.00	−65.85	1449.98	−185.85	−162.39	190.15
BigApple	0.155	0.609	−16.34	226.08	−209.66	31.32	40.00	89.76	1121.88	−150.21	−113.12	315.84
DINOa	0.1522	0.626	−16.16	210.00	−365.42	31.42	50.00	504.96	9316.53	204.96	291.97	714.96
DINOb	0.1525	0.632	−16.21	207.00	−412.46	33.07	70.00	608.70	9692.85	188.70	328.18	815.70
DINOc	0.1519	0.632	−16.22	206.00	−421.37	34.58	90.00	715.40	9846.87	175.40	359.49	921.40
FSU-δ6.2	0.148	0.610	−16.31	229.20	−322.12	32.53	48.21	−311.61	−92.61	−600.87	−533.12	−82.4
FSU-δ6.7	0.148	0.610	−16.31	229.20	−322.12	32.75	53.50	−227.23	673.54	−548.23	−473.04	1.97
FSUGarnet	0.153	0.579	−16.23	229.63	8.47	30.92	50.96	58.31	149.10	−247.45	−249.33	287.94
FSUGarnet+R	0.1527	0.582	−16.18	228.77	−24.37	30.89	55.79	20.00	417.64	−314.74	−308.80	248.77
FSUGold	0.1484	0.610	−16.30	230.00	−523.39	32.59	60.50	−51.27	424.15	−414.27	−276.59	178.73
FSUGold2	0.1505	0.593	−16.28	238.00	−149.49	37.62	112.80	25.21	−165.75	−651.59	−580.74	263.21
FSUGold2+R	0.1522	0.594	−16.22	241.22	−36.17	32.03	57.20	−6.89	971.30	−350.09	−341.51	234.33
HPNL0	0.1477	0.603	−16.10	227.38	−217.51	34.63	78.38	−69.89	488.76	−540.18	−465.20	157.48
HPNL5	0.1486	0.618	−16.18	230.32	−320.74	33.04	52.29	−83.86	1178.98	−397.60	−324.78	146.46
IOPB-I	0.149	0.594	−16.11	222.33	−109.15	33.36	63.70	−38.98	873.02	−421.18	−389.00	183.35
IU-FSU	0.1547	0.609	−16.40	231.30	−289.40	31.30	47.22	28.61	370.02	−254.73	−195.64	259.91
NL3	0.1483	0.595	−16.26	271.50	201.62	37.28	118.18	101.01	181.90	−608.09	−695.86	372.51
PD15	0.1484	0.618	−16.62	229.49	−399.42	35.29	42.60	−56.52	1582.27	−312.10	−237.96	172.97
TAMUC-FSUa	0.149	0.601	−16.23	245.31	−159.85	35.05	82.71	−68.69	382.54	−564.96	−511.07	176.62
TM1	0.145	0.635	−16.23	280.39	−286.69	36.84	110.60	33.50	−65.26	−630.08	−517.00	313.89

Here, E_0 denotes the binding energy per nucleon. The bulk properties are given by coefficients in the power-series expansion of isospin-asymmetric nuclear EoS around ρ_0 in Section 2.4. The K_{asy}, $K_{sat,2}$, and K_N are respectively expressed as $K_{asy} = K_{sym} - 6L$, $K_{sat,2}(= K_\tau) = K_{asy} - J_0 L/K_0$, and $K_N = K_{sym} + K_0$ [147, 148].

coupling constants related to the properties of $N = Z$ finite nuclei and isospin-symmetric nuclear matter—g_σ^2, g_ω^2, g_2, and g_3—are readjusted to closely match the experimental data for the binding energy per nucleon and charge radius of several closed-shell nuclei, as well as to maintain the original K_0 value. The resultant coupling constants and nuclear properties for the FSUGarnet, TAMUC-FSUa, and FSUGold2 series are listed in Table 3. Furthermore, the parameter sets for the FSUGold2 with the δ–N coupling and the quartic self-interaction of ρ meson are also given in Table 4, where the quartic coupling constant, e_3, is varied in the range of $0 \le e_3 \le 800$ with the fixed parameters, $c_3 = 144.12$ and $g_\delta^2 = 300$.

3.2 Finite nuclei

The theoretical predictions for the neutron skin thickness of ^{40}Ca and ^{208}Pb, R_{skin}^{48} and R_{skin}^{208}, in the RMF models are presented in Figure 1, compared with the experimental data: the electric dipole polarizability of ^{48}Ca (RCNP; R_{skin}^{48} =

10.3389/fphy.2024.1531475

TABLE 3 Model parameters and nuclear properties for the extended version of the FSUGarnet, TAMUC-FSUa, and FSUGold2 models.

Models	m_σ (MeV)	g_σ^2	g_ω^2	g_δ^2	g_ρ^2	g_2 (fm^{-1})	g_3	$\Lambda_{\omega\rho}$	E_0 (MeV)	$E_{\rm sym}$ (MeV)	$K_{\rm sym}$ (MeV)
FSUGarnet series (L = 50.96 MeV)											
δ000	496.94	110.35	187.69	0.00	47.97	9.56	−7.12	1555.73	−16.23	30.92	58.31
δ050	496.23	110.06	187.68	50.00	64.41	9.54	−7.11	364.29	−16.25	32.54	39.53
δ100	496.26	110.07	187.68	100.00	95.83	9.54	−7.11	290.10	−16.24	32.50	162.95
δ150	496.41	110.12	187.69	150.00	128.83	9.54	−7.10	274.42	−16.24	32.22	337.44
δ200	496.51	110.16	187.69	200.00	163.34	9.54	−7.10	276.62	−16.23	31.98	548.39
δ250	496.10	109.99	187.69	250.00	199.38	9.53	−7.10	286.98	−16.24	31.85	790.04
δ300	493.90	109.10	187.65	300.00	238.62	9.45	−7.07	303.57	−16.30	32.60	1054.19
TAMUC-FSUa series (L = 82.71 MeV)											
δ000	502.20	106.50	176.18	0.00	24.40	8.83	−6.32	213.86	−16.23	35.05	−68.69
δ050	502.85	106.74	176.19	50.00	53.83	8.84	−6.30	158.60	−16.21	34.55	3.69
δ100	502.75	106.70	176.19	100.00	85.18	8.83	−6.30	159.75	−16.21	34.55	104.58
δ150	502.75	106.70	176.19	150.00	117.17	8.83	−6.30	168.70	−16.21	34.50	233.64
δ200	502.75	106.70	176.19	200.00	149.71	8.83	−6.29	180.42	−16.21	34.35	389.08
δ250	502.70	106.68	176.19	250.00	182.90	8.83	−6.28	193.75	−16.20	34.15	568.48
δ300	502.10	106.44	176.19	300.00	217.36	8.81	−6.28	208.75	−16.22	34.20	767.29
FSUGold2 series (L = 112.80 MeV)											
δ000	497.48	108.07	183.73	0.00	20.15	8.55	−1.02	12.29	−16.28	37.62	25.21
δ050	498.00	108.28	183.74	50.00	50.47	8.56	−1.00	77.62	−16.27	37.55	87.38
δ100	497.96	108.26	183.74	100.00	81.86	8.56	−1.00	109.82	−16.27	37.51	187.87
δ150	499.99	108.27	183.74	150.00	113.85	8.56	−1.00	133.90	−16.27	37.34	320.60
δ200	498.03	108.29	183.74	200.00	146.62	8.56	−1.00	155.39	−16.27	37.12	481.08
δ250	498.09	108.31	183.74	250.00	179.93	8.56	−0.99	175.51	−16.26	36.73	668.45
δ300	497.60	108.12	183.74	300.00	214.65	8.54	−1.01	196.02	−16.27	36.59	876.59

For each series, the parameter c_3 is fixed by the original value shown in Table 1.

0.14–0.20 fm) [107], the complete electric dipole response on ^{208}Pb (RCNP; $R_{\rm skin}^{208} = 0.156^{+0.025}_{-0.021}$ fm) [52], the coherent pion photoproduction cross sections measurement of ^{208}Pb (MAMI; $R_{\rm skin}^{208} = 0.15 \pm 0.03({\rm stat.})^{+0.01}_{-0.03}({\rm sys.})$ fm) [108], and the parity-violating electron scattering off ^{48}Ca (CREX; $R_{\rm skin}^{48} = 0.121 \pm 0.026({\rm exp.}) \pm 0.024({\rm model})$ fm) [50] and off ^{208}Pb (PREX-2; $R_{\rm skin}^{208} = 0.283 \pm 0.071$ fm) [47].

As for the OMEG family, the OMEG0 and OMEG1 give the large values, $R_{\rm skin}^{208} = 0.227$ fm and $R_{\rm skin}^{208} = 0.245$ fm, respectively, which meet the PREX-2 result. The OMEG2 is selected so as to match the predicted result, $R_{\rm skin}^{208} = 0.19 \pm 0.02$ fm, by the assessment of the theoretical uncertainty on parity-violating asymmetry in ^{208}Pb [49]. Meanwhile, the OMEG3 exhibits the small value, $R_{\rm skin}^{48} = 0.161$ fm, which satisfies the experimental result in RCNP and is near the range of CREX experiment, $R_{\rm skin}^{48} = 0.121 \pm 0.035$ fm. We summarize the predictions for the charge radius, $R_{\rm ch}$, neutron skin thickness, $R_{\rm skin}$, and weak radius, $R_{\rm wk}$, of ^{48}Ca and ^{208}Pb in Table 5. We here consider the zero-point energy correction taken from the

TABLE 4 Model parameters and several properties for the FSUGold2 with the δ-N coupling and the quartic self-interaction of ρ meson. We set c_3 = 144.12 and g_δ^2 = 300.00.

Models	m_σ	g_σ^2	g_ω^2	g_ρ^2	g_2	g_3	e_3	$\Lambda_{\omega\rho}$	E_0	$E_{\rm sym}$	$K_{\rm sym}$
	(MeV)				(fm^{-1})				(MeV)	(MeV)	(MeV)
ρ000	497.60	108.12	183.74	214.65	8.54	−1.01	0.00	196.02	−16.27	36.59	876.59
ρ100	497.60	108.11	183.74	214.97	8.54	−1.01	100.00	196.39	−16.27	36.75	875.10
ρ200	497.62	108.12	183.74	215.17	8.55	−1.01	200.00	196.61	−16.27	36.85	874.16
ρ300	497.64	108.13	183.74	215.39	8.55	−1.01	300.00	196.86	−16.27	36.96	873.14
ρ400	497.65	108.13	183.74	215.73	8.55	−1.01	400.00	197.24	−16.27	37.13	871.55
ρ500	497.71	108.16	183.74	215.95	8.55	−1.01	500.00	197.49	−16.27	37.24	870.53
ρ600	497.83	108.20	183.74	216.11	8.55	−1.00	600.00	197.67	−16.27	37.32	869.79
ρ700	497.79	108.19	183.74	216.51	8.55	−1.00	700.00	198.12	−16.27	37.52	867.93
ρ800	497.83	108.21	183.74	216.91	8.55	−1.00	800.00	198.57	−16.27	37.72	866.08

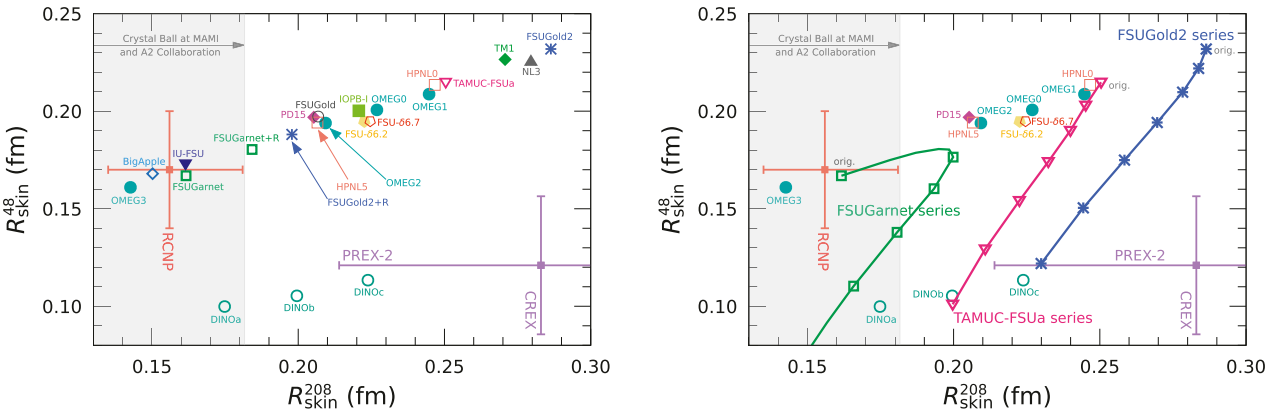

FIGURE 1
Neutron skin thickness of ^{40}Ca and ^{208}Pb, $R^{48}_{\rm skin}$ and $R^{208}_{\rm skin}$. The left panel shows the results from the effective interactions presented in Tables 1, 2. The right panel is for the FSUGarnet, TAMUC-FSUa, and FSUGold2 series in Table 3.

conventional Skyrme Hartree–Fock calculations [9, 109]. The $R_{\rm ch}$ is defined as

$$R_{\rm ch} = \sqrt{R_p^2 + (0.8783)^2}, \tag{86}$$

with R_p being the point proton radius [98].

We see the linear correlation between $R^{48}_{\rm skin}$ and $R^{208}_{\rm skin}$ in the left panel of Figure 1. In general, the larger $R^{48}_{\rm skin}$ and $R^{208}_{\rm skin}$ are obtained by the models with the larger L (see Table 2). To explain the results from RCNP, L should be small such as the OMEG3, BigApple, FSUGarnet, and IU-FSU. In contrast, the DINO family is located far from the points calculated by the other RMF models. As explained in Reed et al. [95], the DINO family expresses the large $K_{\rm sym}$ by means of the huge δ–N and ρ–N couplings. Although it is difficult to support the PREX-2 and CREX results simultaneously, only the DINOc successfully aligns with both data sets. We note that the δ-N coupling and σ-δ mixing affect the charge radii of finite nuclei and hence $R_{\rm skin}$ while they have less influence on the binding energy because we focus on the finite, closed-shell nuclei, ^{16}O, ^{40,48}Ca, ^{68}Ni, ^{90}Zr, ^{100,116,132}Sn, and ^{208}Pb, in the present study [110].

To clarify the effect of δ meson on the characteristics of finite nuclei, we describe the correlation between $R^{48}_{\rm skin}$ and $R^{208}_{\rm skin}$ for the FSUGarnet, TAMUC-FSUa, and FSUGold2 series in the right panel of Figure 1. We also display the calculations based on the other RMF models including the δ meson as well as the σ, ω, and ρ mesons. As shown in Table 3, $K_{\rm sym}$ becomes large as g_δ^2 increases. Consequently, the TAMUC-FSUa, and FSUGold2 series draw the lines from the upper right to the bottom left. In particular, the FSUGold2 with the large δ–N coupling ($g_\delta^2 \geq 250$) supports both experimental data from the parity-violating electron scattering. On the other hand, the FSUGarnet series moves away from the PREX-2 and CREX results when the large g_δ^2 is introduced.

10.3389/fphy.2024.1531475

TABLE 5 Predictions for the charge radius, R_{ch}, neutron skin thickness, R_{skin}, weak radius, R_{wk}, and weak skin thickness, $R_{wk} - R_{ch}$, of ^{48}Ca and ^{208}Pb in fm.

Models	^{48}Ca				^{208}Pb			
	R_{ch}	R_{skin}	R_{wk}	$R_{wk} - R_{ch}$	R_{ch}	R_{skin}	R_{wk}	$R_{wk} - R_{ch}$
OMEG0	3.499	0.201	3.689	0.189	5.514	0.227	5.738	0.223
OMEG1	3.495	0.209	3.693	0.198	5.532	0.245	5.774	0.242
OMEG2	3.500	0.194	3.682	0.183	5.536	0.209	5.741	0.205
OMEG3	3.510	0.161	3.659	0.149	5.549	0.143	5.685	0.136
BigApple	3.496	0.168	3.652	0.156	5.513	0.150	5.657	0.144
DINOa	3.510	0.100	3.597	0.086	5.531	0.175	5.700	0.169
DINOb	3.514	0.105	3.606	0.092	5.531	0.200	5.726	0.195
DINOc	3.519	0.113	3.619	0.100	5.532	0.224	5.752	0.220
FSU-δ6.2	3.501	0.195	3.685	0.183	5.547	0.223	5.766	0.219
FSU-δ6.7	3.502	0.195	3.685	0.184	5.549	0.225	5.770	0.221
FSUGarnet	3.471	0.167	3.626	0.155	5.514	0.162	5.670	0.156
FSUGarnet+R	3.473	0.180	3.643	0.168	5.513	0.184	5.692	0.179
FSUGold	3.479	0.197	3.664	0.186	5.540	0.207	5.742	0.203
FSUGold2	3.469	0.232	3.690	0.221	5.512	0.286	5.797	0.285
FSUGold2+R	3.478	0.188	3.654	0.176	5.509	0.198	5.702	0.193
HPNL0	3.490	0.213	3.692	0.203	5.551	0.247	5.795	0.244
HPNL5	3.493	0.194	3.676	0.183	5.545	0.207	5.747	0.202
IOPB-I	3.493	0.200	3.682	0.189	5.548	0.221	5.765	0.217
IU-FSU	3.473	0.173	3.634	0.161	5.501	0.161	5.656	0.156
NL3	3.490	0.226	3.705	0.215	5.529	0.280	5.807	0.278
PD15	3.520	0.197	3.706	0.186	5.561	0.205	5.762	0.201
TAMUC-FSUa	3.483	0.215	3.687	0.204	5.528	0.250	5.776	0.248
TM1	3.499	0.227	3.715	0.216	5.556	0.271	5.825	0.269
FSUGarnet series								
δ000	3.471	0.167	3.626	0.155	5.514	0.162	5.670	0.156
δ050	3.466	0.176	3.630	0.164	5.496	0.200	5.691	0.195
δ100	3.469	0.160	3.616	0.148	5.497	0.193	5.685	0.188
δ150	3.472	0.138	3.597	0.125	5.480	0.181	5.675	0.175
δ200	3.477	0.110	3.573	0.097	5.504	0.166	5.664	0.160
δ250	3.481	0.078	3.544	0.063	5.508	0.151	5.652	0.144
δ300	3.470	0.050	3.505	0.035	5.509	0.142	5.645	0.136

(Continued on the following page)

TABLE 5 (*Continued*) Predictions for the charge radius, R_{ch}, neutron skin thickness, R_{skin}, weak radius, R_{wk}, and weak skin thickness, $R_{wk}-R_{ch}$, of ^{48}Ca and ^{208}Pb in fm.

Models	^{48}Ca				^{208}Pb			
	R_{ch}	R_{skin}	R_{wk}	$R_{wk}-R_{ch}$	R_{ch}	R_{skin}	R_{wk}	$R_{wk}-R_{ch}$
TAMUC-FSUa series								
δ000	3.483	0.215	3.687	0.204	5.528	0.250	5.776	0.248
δ050	3.484	0.203	3.676	0.192	5.528	0.245	5.770	0.242
δ100	3.487	0.190	3.666	0.179	5.529	0.240	5.765	0.237
δ150	3.491	0.174	3.653	0.162	5.530	0.232	5.759	0.229
δ200	3.495	0.154	3.637	0.142	5.532	0.223	5.751	0.219
δ250	3.501	0.129	3.617	0.116	5.536	0.211	5.742	0.207
δ300	3.506	0.101	3.593	0.087	5.538	0.200	5.734	0.195
FSUGold2 series								
δ000	3.469	0.232	3.690	0.221	5.512	0.286	5.797	0.285
δ050	3.470	0.222	3.681	0.211	5.511	0.284	5.793	0.282
δ100	3.473	0.210	3.672	0.199	5.511	0.278	5.788	0.277
δ150	3.477	0.194	3.660	0.183	5.513	0.270	5.781	0.268
δ200	3.482	0.175	3.645	0.163	5.516	0.258	5.772	0.256
δ250	3.487	0.150	3.625	0.138	5.521	0.244	5.762	0.241
δ300	3.494	0.123	3.603	0.109	5.525	0.230	5.753	0.226
Experiment	3.477	0.121	3.636	0.159	5.501	0.283	5.800	0.299

The PREX-2 and CREX results are also presented.

The density profiles in ^{208}Pb are displayed in Figure 2. We here present the baryon, charge, and weak charge densities, ρ_B ($=\rho_p+\rho_n$), ρ_{ch}, and ρ_W, with the experimental results [47, 111]. The ρ_W is approximately expressed as

$$\rho_W(\boldsymbol{r}) \simeq Q_p\rho_{ch}(\boldsymbol{r}) + Q_n\int d\boldsymbol{r}' G_p^E(|\boldsymbol{r}-\boldsymbol{r}'|)\rho_n(\boldsymbol{r}), \quad (87)$$

with $Q_{p(n)}$ being the proton (neutron) weak charge and G_p^E being the proton electric form factor [112–114]. The OMEG family is calibrated so as to reproduce $-\rho_W$ and ρ_B in ^{208}Pb by the PREX-2 experiment.

In the left panel of Figure 2, we present the density profiles for the OMEG1, DINOc, FSUGarnet. The OMEG1 and FSUGarnet adequately satisfy the density distributions of ρ_{ch} from the elastic electron scattering [111]. On the other hand, the DINOc possesses the instability around the core of nuclei because of the strong δ–N coupling constant [95]. As a result, the density profiles, ρ_B, ρ_{ch}, and ρ_W, show the large density fluctuations around the core.

The effect of δ–N coupling on the density profiles for the FSUGold2 series is illustrated in the right panel of Figure 2. There is almost no difference up to $g_\delta^2=150$. In the case of $g_\delta^2=300$, ρ_{ch} and ρ_W begin to show the instability around the core, but ρ_B still matches the experimental data from PREX-2 [47]. When the larger value, $g_\delta^2>300$, is taken, the unexpectedly large fluctuations of ρ_{ch} and ρ_W emerge around the core, and the wave functions do not converge numerically. In the present study, we thus impose the limit on the δ–N coupling as $g_\delta^2\leq 300$ for the FSUGold2 series. We here comment that this defect can not be solved even if one considers the quartic self-interactions of δ and/or ρ mesons in Equation 3, which less affect R_{skin}^{48} and R_{skin}^{208}.

3.3 Infinite nuclear matter

The δ-meson effect can be clearly seen in the effective nucleon mass, M_N^*, in Equation 3. Displayed in Figure 3 is the density dependence of M_N^* in pure neutron matter for the OMEG family and the FSUGold2 series. When the ρ meson only is included, the RMF model gives the equal effective mass of proton and neutron. However, the iso-scalar δ meson is responsible for the mass splitting between protons and neutrons, where M_p^* is much heavier than M_n^*

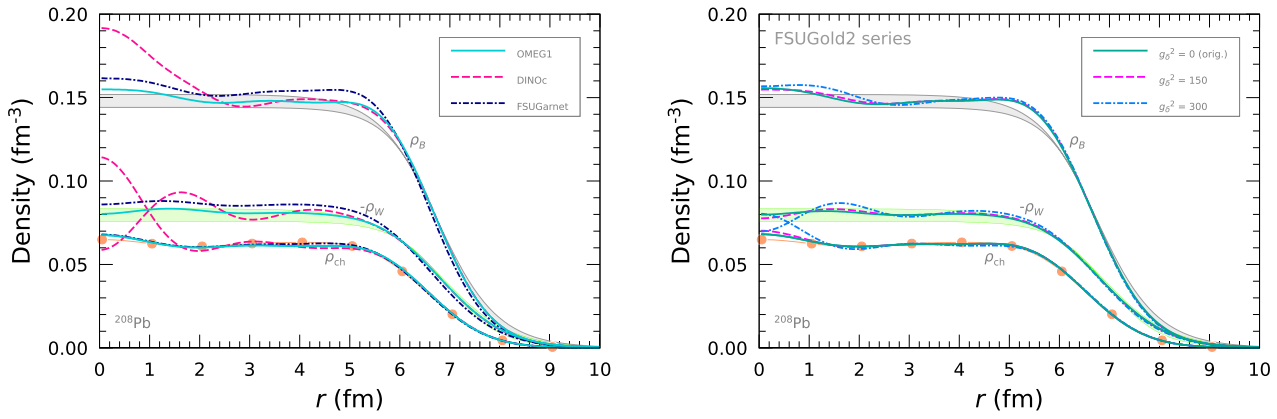

FIGURE 2
Baryon, charge, and weak change densities, ρ_B, ρ_{ch}, and ρ_W, for ^{208}Pb. The density profiles for the OMEG1, DINOc, and FSUGarnet are given in the left panel. The right panel is for the FSUGold2 series.

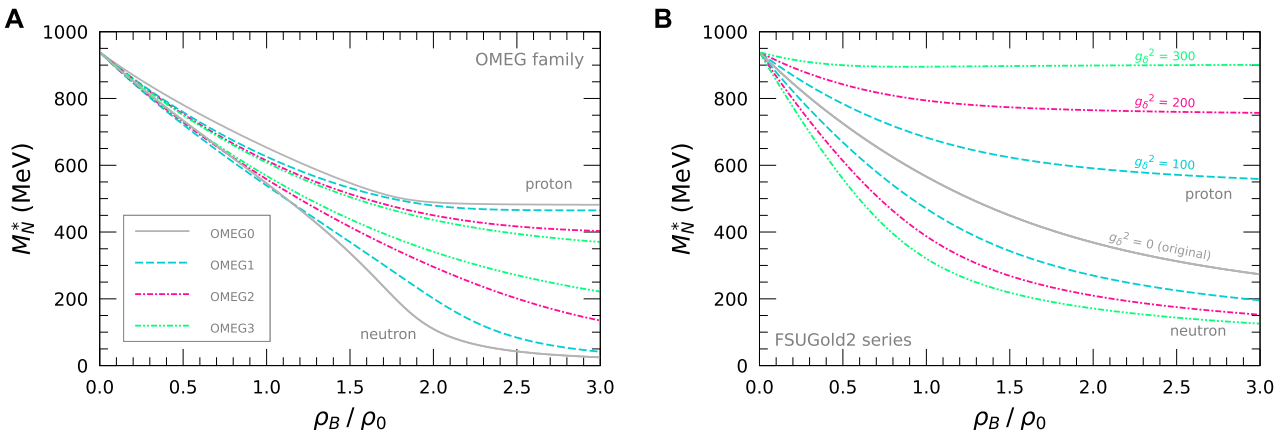

FIGURE 3
Effective nucleon mass, M_N^*, as a function of ρ_B/ρ_0 for the OMEG family **(A)** and the FSUGold2 series **(B)**.

at high densities. Compared with the OMEG family, the FSUGold2 series shows the strong mass splitting, as g_δ^2 increases, even at low densities. It is implied that the neutron distribution is more spread out than the proton one, because M_n^* is lighter, and then, the large fluctuations of ρ_{ch} and ρ_W appear around the core of ^{208}Pb as shown in Figure 2. Due to the δ–N coupling and the σ–δ mixing, M_p^* and M_n^* respectively reach the almost constant values at high densities in all the cases.

The density dependence of nuclear symmetry energy, E_{sym}, in Equation 26 is depicted in Figure 4. We here present the calculations using the OMEG, FSU-δ, and DINO families. Furthermore, we use the conventional ones (the NL3, FSUGold2, TAMUC-FSUa, IOPB-I, and FSUGarnet models). In addition, several experimental or theoretical constraints are presented. Figure 4 highlights significant differences in E_{sym} at high densities, that is, whereas the conventional calculations show a monotonic increase in E_{sym}, the models with the δ meson exhibit more complex behavior. In particular, the DINO family predicts a large E_{sym} above $1.5\rho_0$ as the δ meson amplifies E_{sym} in dense nuclear matter [57]. The OMEG and FSU-δ families, on the other hand, display unusual E_{sym} trends depending on the strength of δ–N coupling and σ–δ mixing. The σ–δ mixing has a weak influence on E_{sym} below ρ_0, but, as discussed by Zabari et al. [56], it becomes substantial above ρ_0. Specifically, the σ–δ mixing reduces E_{sym} at high densities, partially offsetting the increase from the δ–N interaction. Furthermore, in the OMEG0 and FSU-δ6.2, the inflection points appear above ρ_0 and the dip emerges around $2.5\rho_0$–$3.5\rho_0$. This behavior is similar to the cusp in E_{sym} in the skyrmion crystal approach [115, 116] and to the results from the Skyrme Hartree-Fock calculations [117]. We note that, as explained in Section 2.5, the thermodynamic constraint on chemical potential in isospin-asymmetric nuclear matter, $V_\mu(\rho_B, \alpha) > 0$, is satisfied over all densities, namely, $E_{sym}(\rho_B, \alpha) > E_{sym}(\rho_B) > 0$.

Based on the Lorentz decomposition of nucleon self-energy in Section 2.4, E_{sym} is generally divided into the kinetic and potential terms, E_{sym}^{kin} and E_{sym}^{pot}, as $E_{sym} = E_{sym}^{kin} + E_{sym}^{pot}$. In RMF approximation, only the isovector mesons contribute to E_{sym}^{pot} as $E_{sym}^{pot} = E_{sym}^{s} + E_{sym}^{0}$, where the scalar ($s$) and time (0) components, E_{sym}^{s} and E_{sym}^{0}, are respectively given by the δ and ρ mesons. We show the Lorentz

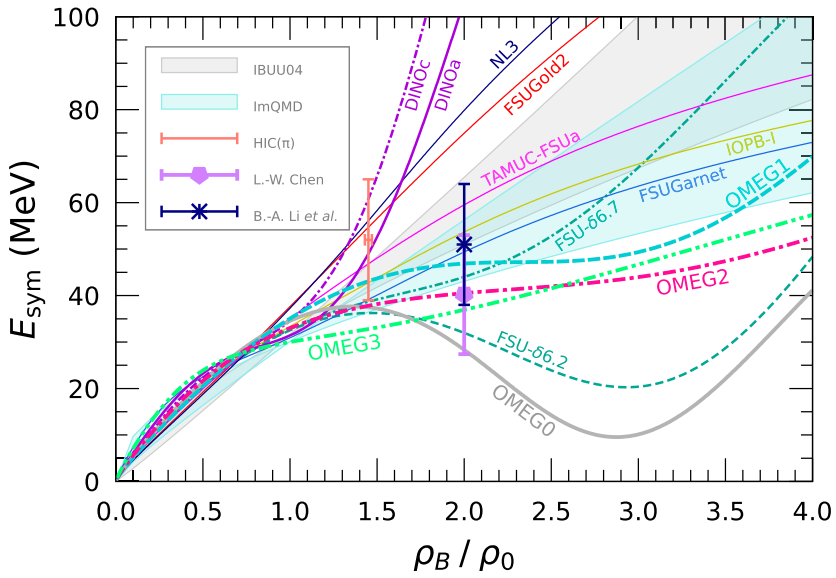

FIGURE 4
Density dependence of nuclear symmetry energy, E_{sym}. The shaded regions are the results from analyses of HIC data using the isospin-dependent Boltzmann-Uehling-Uhlenbec (IBUU04) and improved quantum molecular dynamics (ImQMD) transport models [22, 139, 140]. The recent experimental constraint from the pion emission in heavy-ion reactions is expressed as HIC(π) with $E_{sym}(\rho_B) = 52 \pm 13$ MeV at $\rho_B/\rho_0 = 1.45 \pm 0.2$ [141–143]. We also present two theoretical constraints on the magnitude of E_{sym} at $2\rho_0$ with $E_{sym}(2\rho_0) \simeq 40.2 \pm 12.8$ MeV by Chen [144] and $E_{sym}(2\rho_0) \simeq 51 \pm 13$ MeV by Li et al. [145].

decomposition of E_{sym} for the OMEG family and the FSUGold2 series as a function of ρ_B/ρ_0 in Figure 5. The top panels are the density dependence of E_{sym} and E_{sym}^{kin}. We see that the unique behavior of E_{sym} in the OMEG family is caused by E_{sym}^{pot} because E_{sym}^{kin} is almost the same as in both cases. The contents of E_{sym}^{pot} are given in the middle and bottom panels of Figure 5. It is found that E_{sym}^{s} is negative while E_{sym}^{0} is positive, which is similar to the general understanding of N–N interaction described by the nuclear attractive and repulsive forces. Note that a similar description of E_{sym}^{pot} has been reported using the RMF model with a contact interaction of isovector mesons, where the scalar contribution, $(\bar{\psi}_N \boldsymbol{\tau}_N \psi_N)^2$, is positive while the vector one, $(\bar{\psi}_N \gamma_\mu \boldsymbol{\tau}_N \psi_N)^2$, is negative [118, 119]. It is noticeable that, for the FSUGold2 series, E_{sym}^{s} is strongly influenced by the δ–N coupling above ρ_0, and the contribution of E_{sym}^{s} is small at high densities. Conversely, for the OMEG family, the σ–δ mixing shows less impact on E_{sym}^{s} below ρ_0, but it strongly affects E_{sym}^{s} at high densities. When the absolute value of E_{sym}^{s} is larger than that of E_{sym}^{0}, E_{sym}^{pot} has the rapid reduction, and then E_{sym} shows a dip around $3\rho_0$ as in the cases for the OMEG0 and FSU-δ6.2 in Figure 4.

The EoSs for symmetric nuclear matter and pure neutron matter are displayed in Figure 6 with the constraints on the nuclear EoS extracted from the analyses of particle flow data in HICs [60–62]. In both panels, we show the various EoSs calculated by the OMEG, DINO, and FSU-δ families, and the FSUGarnet and FSUGold2 models. The δ meson does not affect P in symmetric nuclear matter. All the cases except for the OMEG0 are well constructed to match the HIC data in symmetric nuclear matter because of the small K_0. However, the stiffer EoS with $K_0 \simeq 285$ MeV is still acceptable, taking into account the recent simulation of Au+Au collisions [63]. In contrast, the δ meson has a large impact on P in pure neutron matter. The DINOa and DINOc show the hard EoSs, which are far from the constraints from HICs, due to the large δ–N coupling. Meanwhile, the strong σ–δ mixing softens the EoSs extremely for the OMEG and FSU-δ families in the density region from ρ_0 to $2\rho_0$, around which the characteristics of a canonical $1.4\,M_\odot$ neutron star are generally determined.

We present the EoS for pure neutron matter for the FSUGold2 series in Figure 7. In the left panel, the EoS becomes hard with increasing the δ–N coupling, and the EoS with $g_\delta^2 = 300$ exceeds the HIC results as in the cases for the DINO family in Figure 6. Hence, we find that, even if the large δ–N coupling is introduced simply, it is not easy to explain simultaneously both properties of dense nuclear matter and characteristics of finite nuclei for R_{skin}^{48} and R_{skin}^{208} in Figure 1. In order to suppress such excessive stiffness of EoSs for pure neutron matter due to the δ–N coupling, we additionally include the quartic self-interaction of ρ meson in the FSUGold2 model with the upper limit of $g_\delta^2 = 300$ (see Table 4), given in the right panel of Figure 7. The EoS is soft and again reaches the upper edge of the constraint from HICs with increasing the quartic coupling, e_3, whose effect is almost imperceptible below ρ_0.

3.4 Neutron star physics

In studying neutron star physics, the EoS for non-uniform matter is additionally required as well as that for uniform nuclear matter since the radius of a neutron star is remarkably sensitive to the nuclear EoS at very low densities [120]. In the present study, to cover the crust region, we adopt the MYN13 EoS, in which nuclei are taken into consideration using the Thomas-Fermi calculation in non-uniform matter and the EoS for infinite nuclear matter is constructed with the relativistic Hartree-Fock calculation [80, 81,

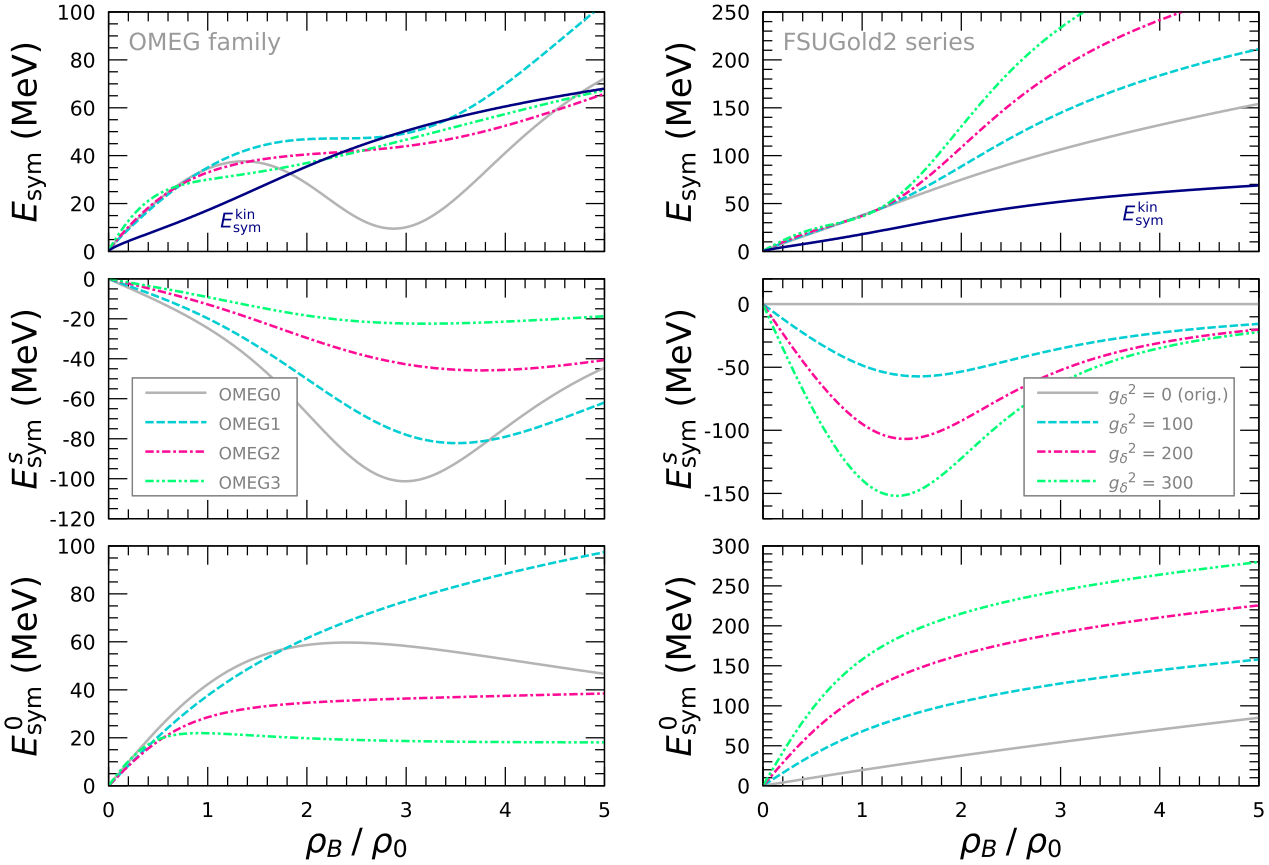

FIGURE 5
Lorentz decomposition of nuclear symmetry energy, E_{sym}, for the OMEG family (left panels) and the FSUGold2 series (right panels). The total E_{sym} and the kinetic term, E^{kin}_{sym}, are presented in the top panels. The scalar (time) component of potential term, E^{s}_{sym} (E^{0}_{sym}), is given in the middle (bottom) panels.

121, 122]. We list in Table 6 the predicted stellar properties, which are calculated by solving the Tolman–Oppenheimer–Volkoff (TOV) equation [123, 124].

There are three methods used widely to determine the crust-core transition density, ρ_t [125]: the thermo-dynamical method, the dynamical method, and the random-phase-approximation method. We employ the first method in the present study. As explained in Section 2.5, the stability of nuclear and neutron star matter is determined by the constraints on chemical potential and pressure, $V_\mu(\rho_B, \alpha) > 0$ and $V_P(\rho_B, \alpha) > 0$, in the first law of thermodynamics. Since the proton fraction, Y_p, is supposed to be small in the crust region, the second-order Taylor series approximation of the nuclear EoS is generally adopted in the density derivative of baryon pressure, $(\partial P_B/\partial \rho_B)_\mu$, in Equation 28 [83]. However, it has been reported that the parabolic approximation of isospin-asymmetric nuclear EoS may be misleading as regards the predictions for ρ_t [89]. We thus employ the exact nuclear EoS to calculate V_P defined in Equation 29.

We summarize the results of ρ_t in the second column of Table 6. Compared with the results from the Taylor series expansion, the our results settle between the second-order and fourth-order calculations. For example, for the FSUGold, the exact value is ρ_t = 0.079 fm^{-3} while the second-order (fourth-order) result is ρ_t^{2nd} = 0.089 (ρ_t^{4th} = 0.051) fm^{-3} (see Table 2 in Routray et al. [89]). In addition, the current results are almost the same as the transition density from the pasta phase to the homogeneous nuclear matter in the model calculation with Thomas-Fermi approximation [126]. The EoS for neutron star matter in the OMEG family is presented in Figure 8. The crust-core phase transition occurs at $V_P = 0$, which is also described in the left panel of Figure 9. As it is well known, the EoS with larger L gives the smaller ρ_t [127].

Since the large σ–δ mixing enhances the rapid reduction of E_{sym} around $3\rho_0$ as shown in Figure 4, we have to investigate the stability of neutron star matter. Similar to the crust-core phase transition, we adopt the thermo-dynamical method. It is especially important to apply the exact nuclear EoS to V_P because Y_p is by no means small and the Taylor series expansion is prohibited at high densities. It is found that the constraint on chemical potential, $V_\mu > 0$, is always satisfied as E_{sym} is positive at any densities. Hence, all we have to do is check the thermodynamic stability of pressure, V_P. In Figure 9, we show V_P in neutron star matter. In general, V_P changes from negative to positive at ρ_t, and the stable EoS possesses $V_P > 0$ even at high densities. Despite the OMEG0 give a strong concavity in E_{sym} by the σ–δ mixing, it satisfies the thermodynamic stability. In the right panel of Figure 9, we show V_P for the FSUGold2 series. The neutron star matter keeps $V_P > 0$ when the δ–N coupling only is included, whereas the large quartic self-interaction of ρ meson, e_3, makes the matter unstable. Though the quartic ρ-meson self-interaction is useful to figure out the HIC data as mentioned in the

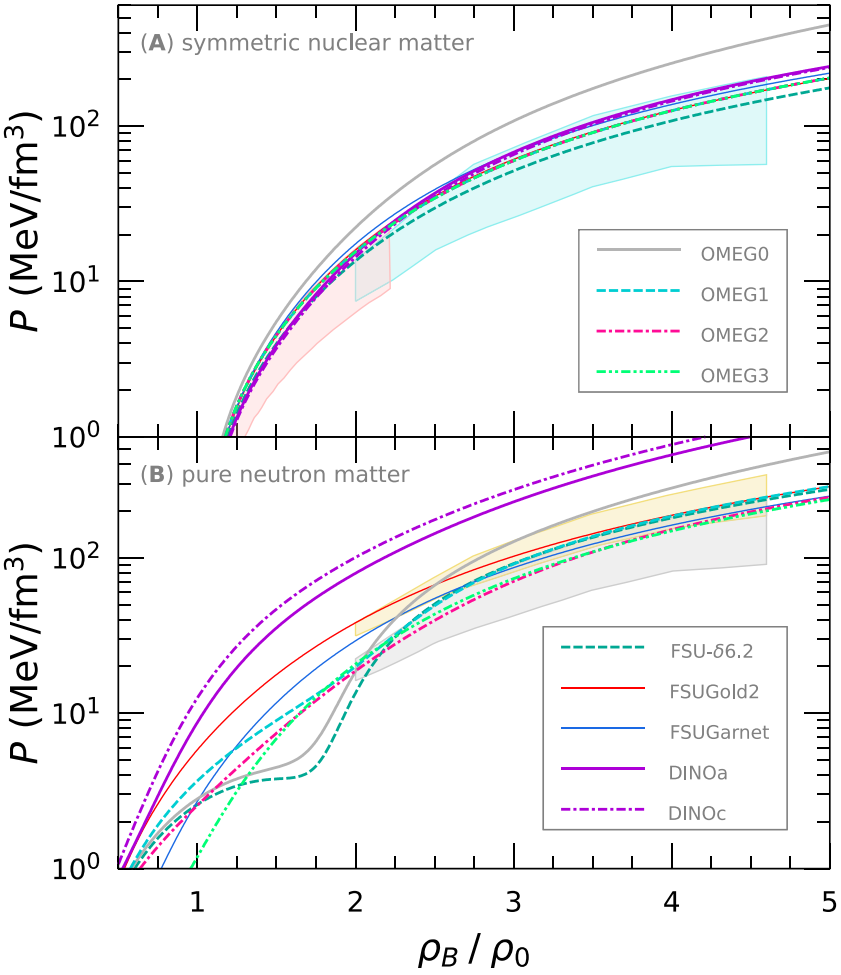

FIGURE 6
EoS—pressure, P, as a function of ρ_B/ρ_0—for **(A)** symmetric nuclear matter and for **(B)** pure neutron matter. The shaded areas represent the constraints from elliptical flow data [60] and kaon production data [61, 62].

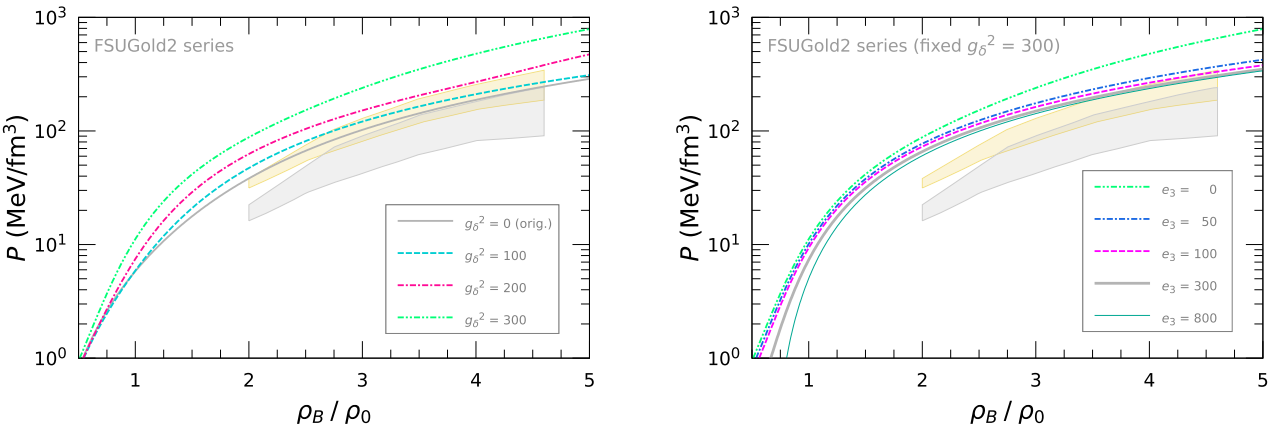

FIGURE 7
EoS for pure neutron matter for the FSUGold2 series. The left panel shows the dependence of δ–N coupling square, g_δ^2. In the right panel, the influence of quartic ρ-meson self-interaction, e_3, is presented with the fixed parameter of $g_\delta^2 = 300$ (see Table 4).

10.3389/fphy.2024.1531475

TABLE 6 Properties of neutron stars.

Models	ρ_t (fm^{-1})	$R_{1.4}$ (km)	$\rho_{1.4}$ (fm^{-1})	$\Lambda_{1.4}$	$M_{\max}$ ($M_\odot$)	$R_{\max}$ (km)	$\rho_{\max}$ (fm^{-1})	$\Lambda_{\max}$
OMEG0	0.093	12.43	0.359	498	2.61	12.16	0.772	4
OMEG1	0.079	12.76	0.402	515	2.13	11.70	0.917	14
OMEG2	0.093	12.40	0.428	458	2.07	11.31	0.980	13
OMEG3	0.104	12.40	0.409	462	2.07	11.39	0.962	14
BigApple	0.096	13.03	0.329	677	2.60	12.38	0.759	5
DINOa	0.092	14.11	0.307	1047	2.17	12.30	0.854	16
DINOb	0.087	14.37	0.306	1136	2.15	12.26	0.870	16
DINOc	0.083	14.63	0.301	1237	2.15	12.30	0.871	16
FSU-δ6.2	0.083	12.08	0.409	416	2.10	11.53	0.922	16
FSU-δ6.7	0.082	12.82	0.386	573	2.05	11.76	0.917	20
FSUGarnet	0.084	12.87	0.382	596	2.07	11.66	0.932	17
FSUGarnet+R	0.083	12.94	0.384	616	2.06	11.66	0.938	18
FSUGold	0.079	12.32	0.520	400	1.72	10.80	1.156	32
FSUGold2	0.061	14.00	0.351	873	2.07	12.09	0.904	19
FSUGold2+R	0.087	13.19	0.347	715	2.26	12.10	0.848	12
HPNL0	0.072	13.32	0.383	674	2.03	11.74	0.946	19
HPNL5	0.088	12.76	0.408	551	2.01	11.43	0.980	18
IOPB-I	0.081	13.21	0.362	693	2.15	11.92	0.890	15
IU-FSU	0.088	12.49	0.433	482	1.94	11.19	1.027	19
NL3	0.063	14.68	0.272	1255	2.77	13.30	0.668	4
PD15	0.094	12.49	0.434	488	1.92	11.19	1.026	21
TAMUC-FSUa	0.073	13.48	0.365	725	2.10	11.92	0.909	17
TM1	0.068	14.31	0.320	1038	2.18	12.37	0.852	16
FSUGarnet series								
δ000	0.084	12.87	0.382	596	2.07	11.66	0.932	17
δ050	0.094	13.09	0.360	681	2.10	11.91	0.893	18
δ100	0.097	13.37	0.336	784	2.13	12.15	0.859	19
δ150	0.097	13.62	0.318	893	2.14	12.31	0.841	20
δ200	0.097	13.82	0.307	973	2.13	12.40	0.833	21
δ250	0.096	13.96	0.301	1031	2.13	12.42	0.834	22
δ300	0.095	14.02	0.300	1059	2.12	12.39	0.840	22

(Continued on the following page)

TABLE 6 (*Continued*) Properties of neutron stars.

Models	ρ_t (fm^{-1})	$R_{1.4}$ (km)	$\rho_{1.4}$ (fm^{-1})	$\Lambda_{1.4}$	M_{max} ($M_\odot$)	R_{max} (km)	ρ_{max} (fm^{-1})	Λ_{max}
TAMUC-FSUa series								
δ000	0.073	13.48	0.365	725	2.10	11.92	0.909	17
δ050	0.076	13.72	0.338	850	2.14	12.19	0.867	17
δ100	0.080	13.94	0.318	947	2.16	12.39	0.839	18
δ150	0.083	14.15	0.302	1073	2.17	12.53	0.824	19
δ200	0.085	14.33	0.292	1158	2.17	12.60	0.818	20
δ250	0.086	14.48	0.285	1249	2.16	12.63	0.817	21
δ300	0.086	14.58	0.283	1276	2.16	12.63	0.820	21
FSUGold2 series								
δ000	0.061	14.00	0.351	873	2.07	12.09	0.904	19
δ050	0.064	14.13	0.335	950	2.08	12.25	0.881	21
δ100	0.069	14.29	0.318	1045	2.09	12.39	0.861	22
δ150	0.074	14.45	0.304	1151	2.10	12.49	0.849	23
δ200	0.078	14.58	0.295	1227	2.10	12.54	0.844	24
δ250	0.080	14.68	0.289	1297	2.09	12.56	0.843	24
δ300	0.082	14.74	0.287	1334	2.08	12.55	0.846	24

We calculate the crust-core transition density, ρ_t, and the observables at the canonical- and maximum-mass points.

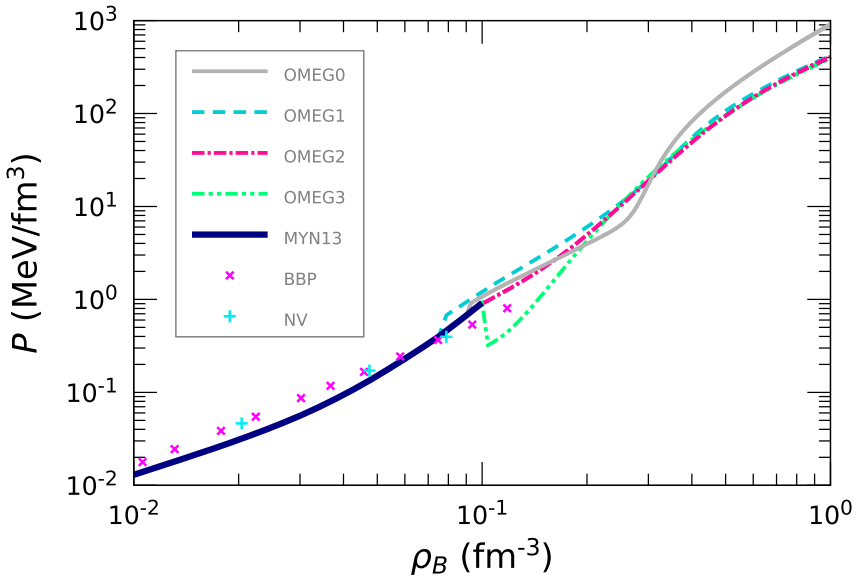

FIGURE 8
EoS for neutron star matter for the OMEG family. The inner-crust region is described by the EoSs of MYN13 [121], BBP [1], and NV [146].

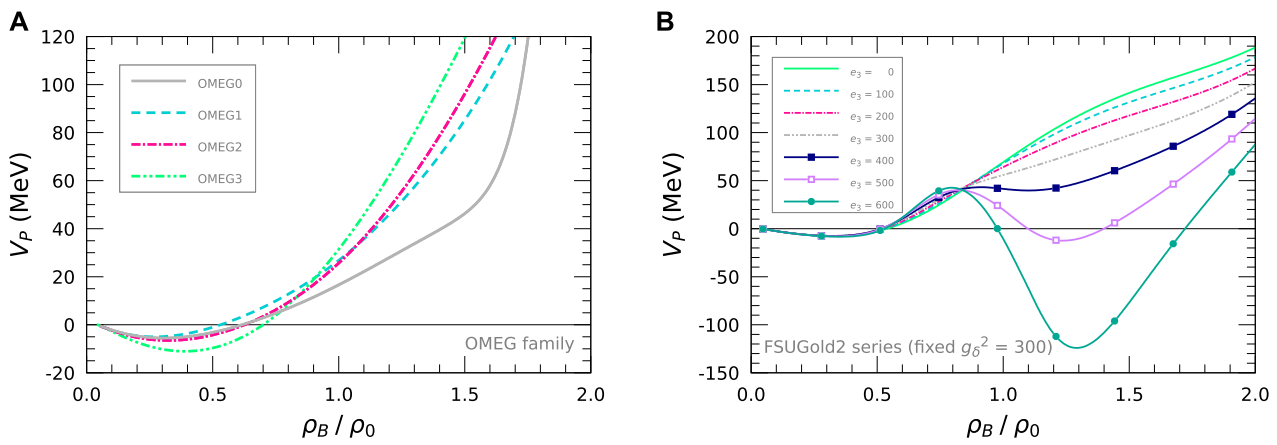

FIGURE 9
Thermodynamic stability of pressure, V_p, in neutron star matter for the OMEG family **(A)** and for the FSUGold2 series with the fixed parameter of g_δ^2 = 300 **(B)**.

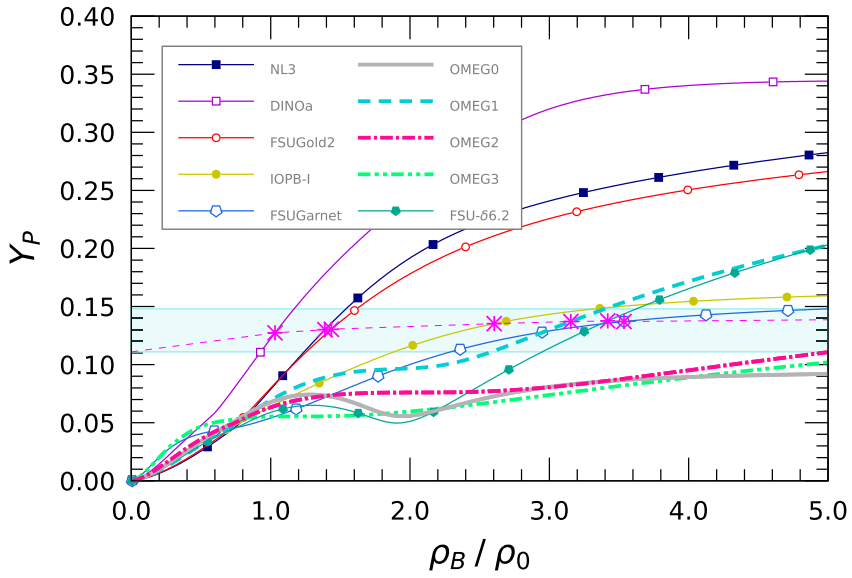

FIGURE 10
Proton fraction, Y_p ($= \rho_p/\rho_B$), in neutron star matter. The shaded band is the threshold for the direct URCA process [118, 128]. The asterisks indicate the densities at which the direct URCA process actually begins.

right panel of Figure 7, the large value of e_3 is unfavorable to the neutron star physics.

We illustrate in Figure 10 the proton fraction, Y_p, in neutron star matter with the threshold for the direct URCA process. The direct URCA process is visible only when Y_p is large enough to conserve momentum in β-equilibrated matter, in which the Fermi momenta of neutrons, protons, and electron must satisfy the relation: $k_{F_n} \leq k_{F_p} + k_{F_e}$. Hence, Y_p can be estimated as $0.111 \leq Y_p \leq 0.148$, above which the direct URCA cooling occurs [118, 128, 129]. We find that as ρ_B increases, the threshold of Y_p for the direct URCA process shifts toward the upper boundary where muons are present. The Y_p for the DINOa grows quickly with increasing ρ_B due to the large δ–N coupling, and then the direct URCA process is allowed sufficiently at $2\rho_0$, which corresponds to the core density of a canonical $1.4M_\odot$ neutron star. Conversely, in the OMEG and FSU-δ families, the σ–δ mixing suppresses Y_p, and then delays the direct URCA process. Particularly, the direct URCA process never occurs for the OMEG0, OMEG2, and OMEG3 in the current density region, and thus the so-called modified URCA process, which is the standard model of neutron-star coolings, mainly takes place for the neutrino emission [130]. Alternatively, the possibility of exotic degrees of freedom in the core of a neutron star, such as hyperons, quarks, gluons and/or some unusual condensations of boson-like matter, should be taken into account to understand the rapid neutron star cooling.

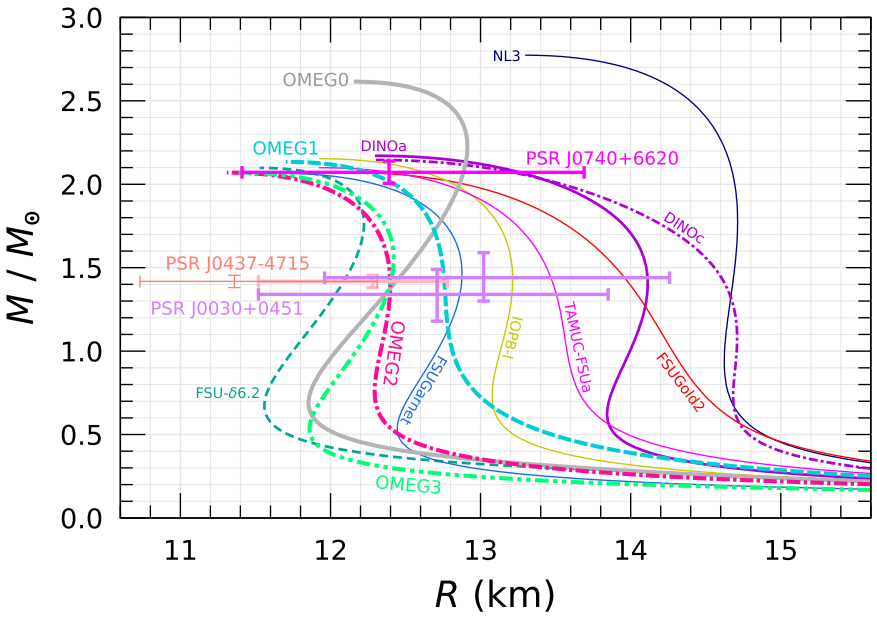

FIGURE 11
Mass–radius relations of neutron stars. The NICER observation data are supplemented by the constraints from PSR J0030+0451 ($1.44^{+0.15}_{-0.14}$ $M_\odot$ and $13.02^{+1.24}_{-1.06}$ km, and $1.34^{+0.15}_{-0.16}$ $M_\odot$ and $12.71^{+1.14}_{-1.19}$ km) [29, 31], PSR J0740+6620 ($2.072^{+0.067}_{-0.066}$ $M_\odot$ and $12.39^{+1.30}_{-0.98}$ km) [32, 64, 65], and PSR J0437–4715 ($12.28^{+0.50}_{-0.76}$ km at 1.4 $M_\odot$, and 1.418 ± 0.037 $M_\odot$ and $11.36^{+0.95}_{-0.63}$ km) [131, 132].

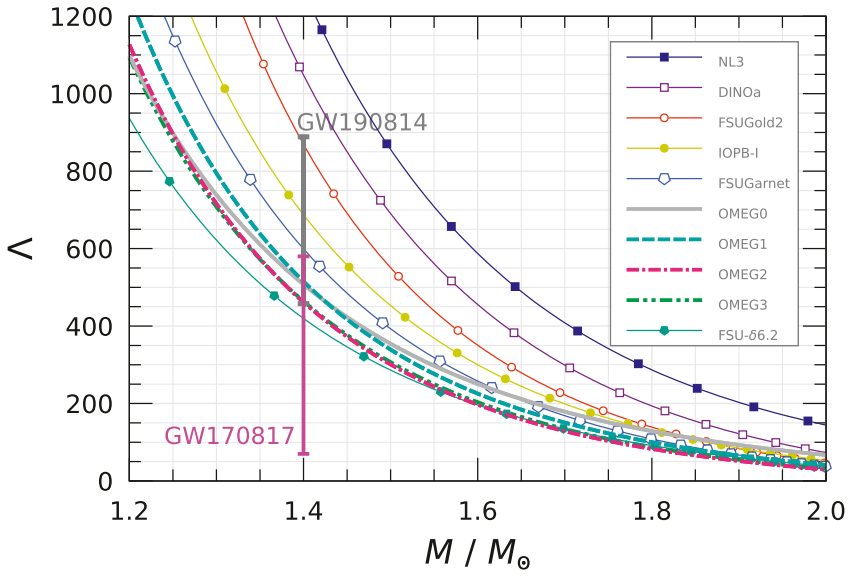

FIGURE 12
Dimensionless tidal deformability, Λ, of neutron stars. We present the constraints on $\Lambda_{1.4}$ from the binary merger events, GW170817 ($\Lambda_{1.4} = 190^{+390}_{-120}$) [34] and GW190814 ($\Lambda_{1.4} = 616^{+273}_{-158}$) [93].

The mass(M)–radius(R) relations of neutron stars are displayed in Figure 11. We here show the astrophysical constraints from the NICER observations: PSR J0030+0451 [29, 31], PSR J0740+6620 [32, 64, 65], and PSR J0437–4715 [131, 132]. According to the observation from PSR J0740+6620, the maximum mass of a neutron star, $M_{\rm max}$, should be larger than $2M_\odot$. Thus the EoS involving the large R, such as the NL3, is ruled out. It is found that the large δ–N coupling affects the large R in the DINO family, whereas the

σ–δ mixing makes R small in the OMEG family. In particular, though the DINOa and OMEG0 have the same L as $L = 50$ MeV, their M–R relations are completely different and the difference of R at canonical-mass point reads approximately 1.7 km (see also Table 6). The OMEG family can support not only the NICER constraint on $R_{1.4}$ from PSR J0030+0451 but also that from PSR J0437−4715, which is the latest result based on new chiral effective field theory inputs [131].

The dimensionless tidal deformability, Λ, of neutron stars is displayed in Figure 12 as a function of $M/M_\odot$. The Λ is defined as $\Lambda = \frac{2}{3}k_2(R/M)^5$ with k_2 being the second Love number [36, 37]. The astrophysical constraints on Λ at the canonical-mass point, $\Lambda_{1.4}$, from the binary merger events detected by the Advanced LIGO and Advanced Virgo observatories are also presented as follows: $\Lambda_{1.4} = 190^{+390}_{-120}$ for GW170817 [34] and $\Lambda_{1.4} = 616^{+273}_{-158}$ for GW190814 [93]. As explained in Miyatsu et al. [57], the δ–N coupling enlarges Λ for the DINOa, and then $\Lambda_{1.4}$ lies far from the constraints on $\Lambda_{1.4}$ from GW190814. On the other hand, the σ–δ mixing has a promising effect on Λ, and thus the OMEG family sufficiently matches the severe constraints from both GW170817 and GW190814.

4 Summary and conclusion

We have developed a new family of nuclear EoSs, referred to as the OMEG family, using the RMF model with non-linear couplings between the isoscalar and isovector mesons. In addition to the σ, ω, and ρ mesons, we have also included the δ meson to examine the ground-state properties of finite, closed-shell nuclei as well as the characteristics of nuclear and neutron star matter. Specifically, we have investigated the effects of δ–N coupling and σ–δ mixing on the EoS for both nuclear and neutron star matter. The model parameters for the OMEG family have been calibrated so as to satisfy the constraints from the particle flow data in HICs [60–62], the observed neutron-star mass of PSR J0740+6620 [32, 64, 65], and the dimensionless tidal deformability, $\Lambda_{1.4}$, from the neutron star merger, GW170817 [34], as well as the results from the PREX-2 and CREX experiments [47, 50].

It has been found that the δ–N coupling and the σ–δ mixing significantly influence the properties of isospin-asymmetric nuclear matter and finite nuclei, playing a crucial role in reconciling terrestrial experiments with astrophysical observations of neutron stars. The strong δ–N coupling for the FSUGold2 series can simultaneously explain the large $R^{208}_{\rm skin}$ and the small $R^{48}_{\rm skin}$ measured by the PREX-2 and CREX experiments. However, it seems difficult that the FSUGold2 series satisfy the combined constraints from the particle flow data in HICs and astrophysical observations, such as the EoS for pure neutron matter and the Λ of neutron stars. Even with the inclusion of quartic ρ-meson self-interaction in the FSUGold2 series, both experimental and observational results can not be understood, because the large e_3 destabilizes neutron star matter. In contrast, the OMEG family can satisfy the recent measurement of $R_{1.4} = 12.28^{+0.50}_{-0.76}$ km for PSR J0437−4715 from NICER [131] and the stringent constraint on $\Lambda_{1.4} = 190^{+390}_{-120}$ from GW170817 [34]. This is attributed to the σ–δ mixing, which suppresses $E_{\rm sym}$ above $2\rho_0$, resulting in a softer nuclear EoS in the density region corresponding to the core density of the canonical neutron stars.

In a future work, we plan to extend the present study to global calculations of finite nuclei properties covered the periodic table, aiming to achieve well-calibrated parameter sets for the RMF models. Finally, we comment that the further theoretical studies are necessary to reconcile the $R_{\rm skin}$ measured by proton (in)elastic scattering with that obtained from parity-violating electron scattering. In particular, it is very significant to investigate the discrepancy between the PREX-2 data [47] and the results from RCNP [51, 52] and MAMI [108]. It is also essential to consider the effect of isospin symmetry breaking on asymmetric nuclear matter from the quark level [133–138].

Author contributions

TM: Writing–original draft, Writing–review and editing. M-KC: Writing–review and editing. KK: Writing–review and editing. KS: Writing–review and editing.

Funding

The author(s) declare that financial support was received for the research, authorship, and/or publication of this article. This work was supported by the National Research Foundation of Korea (Grant Nos. RS-2023-00242196, NRF-2021R1A6A1A03043957, NRF-2020R1A2C3006177, and NRF-2018R1A5A1025563).

Acknowledgments

TM would like to thank H. Sagawa and G. Colò for informative discussions of the neutron skin thickness of heavy nuclei.

Conflict of interest

The authors declare that the research was conducted in the absence of any commercial or financial relationships that could be construed as a potential conflict of interest.

Generative AI statement

The author(s) declare that no Generative AI was used in the creation of this manuscript.

Publisher's note

References

1. Baym G, Bethe HA, Pethick C. Neutron star matter. *Nucl Phys A* (1971) 175:225–71. doi:10.1016/0375-9474(71)90281-8

2. Bethe HA, Brown GE, Applegate J, Lattimer JM. Equation of state in the gravitational collapse of stars. *Nucl Phys A* (1979) 324:487–533. doi:10.1016/0375-9474(79)90596-7

3. Lattimer JM, Swesty FD. A Generalized equation of state for hot, dense matter. *Nucl Phys A* (1991) 535:331–76. doi:10.1016/0375-9474(91)90452-C

4. Glendenning NK, Moszkowski SA. Reconciliation of neutron star masses and binding of the lambda in hypernuclei. *Phys Rev Lett* (1991) 67:2414–7. doi:10.1103/PhysRevLett.67.2414

5. Machleidt R, Holinde K, Elster C. The bonn meson exchange model for the nucleon nucleon interaction. *Phys Rept* (1987) 149:1–89. doi:10.1016/S0370-1573(87)80002-9

6. Machleidt R. The Meson theory of nuclear forces and nuclear structure. *Adv Nucl Phys* (1989) 19:189–376. doi:10.1007/978-1-4613-9907-0_2

7. Serot BD, Walecka JD. The relativistic nuclear many body problem. *Adv Nucl Phys* (1986) 16:1–327.

8. Boguta J, Bodmer AR. Relativistic calculation of nuclear matter and the nuclear surface. *Nucl Phys A* (1977) 292:413–28. doi:10.1016/0375-9474(77)90626-1

9. Sugahara Y, Toki H. Relativistic mean field theory for unstable nuclei with nonlinear sigma and omega terms. *Nucl Phys A* (1994) 579:557–72. doi:10.1016/0375-9474(94)90923-7

10. Mueller H, Serot BD. Relativistic mean field theory and the high density nuclear equation of state. *Nucl Phys A* (1996) 606:508–37. doi:10.1016/0375-9474(96)00187-X

11. Horowitz CJ, Piekarewicz J. The Neutron radii of Pb-208 and neutron stars. *Phys Rev C* (2001) 64:062802. doi:10.1103/PhysRevC.64.062802

12. Oertel M, Hempel M, Klähn T, Typel S. Equations of state for supernovae and compact stars. *Rev Mod Phys* (2017) 89:015007. doi:10.1103/RevModPhys.89.015007

13. Alford MG, Brodie L, Haber A, Tews I. Relativistic mean-field theories for neutron-star physics based on chiral effective field theory. *Phys Rev C* (2022) 106:055804. doi:10.1103/PhysRevC.106.055804

14. Patra NK, Venneti A, Imam SMA, Mukherjee A, Agrawal BK. Systematic analysis of the impacts of symmetry energy parameters on neutron star properties. *Phys Rev C* (2023) 107:055804. doi:10.1103/PhysRevC.107.055804

15. Stone JR. Nuclear physics and astrophysics constraints on the high density matter equation of state. *Universe* (2021) 7:257. doi:10.3390/universe7080257

16. Stone JR. Nuclear symmetry energy in strongly interacting matter: past, present and future. *Symmetry* (2024) 16:1038. doi:10.3390/sym16081038

17. Zhou J, Xu J, Papakonstantinou P. Bayesian inference of neutron-star observables based on effective nuclear interactions. *Phys Rev C* (2023) 107:055803. doi:10.1103/PhysRevC.107.055803

18. Sun B, Bhattiprolu S, Lattimer JM. Compiled properties of nucleonic matter and nuclear and neutron star models from nonrelativistic and relativistic interactions. *Phys Rev C* (2024) 109:055801. doi:10.1103/PhysRevC.109.055801

19. Li B-A, Chen L-W, Ko CM. Recent progress and new challenges in isospin physics with heavy-ion reactions. *Phys Rept* (2008) 464:113–281. doi:10.1016/j.physrep.2008.04.005

20. Lattimer JM. Symmetry energy in nuclei and neutron stars. *Nucl Phys A* (2014) 928:276–95. doi:10.1016/j.nuclphysa.2014.04.008

21. Typel S, Brown BA. Neutron radii and the neutron equation of state in relativistic models. *Phys Rev C* (2001) 64:027302. doi:10.1103/PhysRevC.64.027302

22. Tsang MB, Zhang Y, Danielewicz P, Famiano M, Li Z, Lynch WG, et al. Constraints on the density dependence of the symmetry energy. *Phys Rev Lett* (2009) 102:122701. doi:10.1103/PhysRevLett.102.122701

23. Tsang MB, Stone JR, Camera F, Danielewicz P, Gandolfi S, Hebeler K, et al. Constraints on the symmetry energy and neutron skins from experiments and theory. *Phys Rev C* (2012) 86:015803. doi:10.1103/PhysRevC.86.015803

24. Zhang N-B, Li B-A. Impact of NICER's radius measurement of PSR J0740+6620 on nuclear symmetry energy at suprasaturation densities. *Astrophys J* (2021) 921:111. doi:10.3847/1538-4357/ac1e8c

25. Richter J, Li B-A. Empirical radius formulas for canonical neutron stars from bidirectionally selecting features of equations of state in extended Bayesian analyses of observational data. *Phys Rev C* (2023) 108:055803. doi:10.1103/PhysRevC.108.055803

26. Xie W-J, Li B-A, Zhang N-B. Impact of the newly revised gravitational redshift of x-ray burster GS 1826-24 on the equation of state of supradense neutron-rich matter. *Phys Rev D* (2024) 110:043025. doi:10.1103/PhysRevD.110.043025

27. Demorest P, Pennucci T, Ransom S, Roberts M, Hessels J. Shapiro delay measurement of A two solar mass neutron star. *Nature* (2010) 467:1081–3. doi:10.1038/nature09466

28. Arzoumanian Z, Brazier A, Burke-Spolaor S, Chamberlin S, Chatterjee S, Christy B, et al. The NANOGrav 11-year data set: high-precision timing of 45 millisecond pulsars. *Astrophys J Suppl* (2018) 235:37. doi:10.3847/1538-4365/aab5b0

29. Miller MC, Lamb FK, Dittmann AJ, Bogdanov S, Arzoumanian Z, Gendreau KC, et al. PSR J0030+0451 mass and radius from NICER data and implications for the properties of neutron star matter. *Astrophys J Lett* (2019) 887:L24. doi:10.3847/2041-8213/ab50c5

30. Miller MC, Lamb FK, Dittmann AJ, Bogdanov S, Arzoumanian Z, Gendreau KC, et al. The radius of PSR J0740+6620 from NICER and XMM-Newton data. *Astrophys J Lett* (2021) 918:L28. doi:10.3847/2041-8213/ac089b

31. Riley TE, Watts AL, Bogdanov S, Ray PS, Ludlam RM, Guillot S, et al. A NICER view of PSR J0030+0451: millisecond pulsar parameter estimation. *Astrophys J Lett* (2019) 887:L21. doi:10.3847/2041-8213/ab481c

32. Riley TE, Watts AL, Ray PS, Bogdanov S, Guillot S, Morsink SM, et al. A NICER view of the massive pulsar PSR J0740+6620 informed by radio timing and XMM-Newton spectroscopy. *Astrophys J Lett* (2021) 918:L27. doi:10.3847/2041-8213/ac0a81

33. Abbott BP, Abbott R, Abbott TD, Acernese F, Ackley K, Adams C, et al. GW170817: observation of gravitational waves from a binary neutron star inspiral. *Phys Rev Lett* (2017) 119:161101. doi:10.1103/PhysRevLett.119.161101

34. Abbott BP, Abbott R, Abbott TD, Acernese F, Ackley K, Adams C, et al. GW170817: measurements of neutron star radii and equation of state. *Phys Rev Lett* (2018) 121:161101. doi:10.1103/PhysRevLett.121.161101

35. Abbott BP, Abbott R, Abbott TD, Acernese F, Ackley K, Adams C, et al. Properties of the binary neutron star merger GW170817. *Phys Rev X* (2019) 9:011001. doi:10.1103/PhysRevX.9.011001

36. Hinderer T. Tidal Love numbers of neutron stars. *Astrophys J* (2008) 677:1216–20. Erratum: Astrophys.J. 697, 964 (2009) doi:10.1086/533487

37. Hinderer T, Lackey BD, Lang RN, Read JS. Tidal deformability of neutron stars with realistic equations of state and their gravitational wave signatures in binary inspiral. *Phys Rev D* (2010) 81:123016. doi:10.1103/PhysRevD.81.123016

38. Annala E, Gorda T, Kurkela A, Vuorinen A. Gravitational-wave constraints on the neutron-star-matter equation of state. *Phys Rev Lett* (2018) 120:172703. doi:10.1103/PhysRevLett.120.172703

39. Lim Y, Holt JW. Neutron star tidal deformabilities constrained by nuclear theory and experiment. *Phys Rev Lett* (2018) 121:062701. doi:10.1103/PhysRevLett.121.062701

40. Most ER, Weih LR, Rezzolla L, Schaffner-Bielich J. New constraints on radii and tidal deformabilities of neutron stars from GW170817. *Phys Rev Lett* (2018) 120:261103. doi:10.1103/PhysRevLett.120.261103

41. Raithel C, Özel F, Psaltis D. Tidal deformability from GW170817 as a direct probe of the neutron star radius. *Astrophys J Lett* (2018) 857:L23. doi:10.3847/2041-8213/aabcbf

42. Alam N, Agrawal BK, Fortin M, Pais H, Providência C, Raduta AR, et al. Strong correlations of neutron star radii with the slopes of nuclear matter incompressibility and symmetry energy at saturation. *Phys Rev C* (2016) 94:052801. doi:10.1103/PhysRevC.94.052801

43. Hu J, Bao S, Zhang Y, Nakazato K, Sumiyoshi K, Shen H. Effects of symmetry energy on the radius and tidal deformability of neutron stars in the relativistic mean-field model. *PTEP* (2020) 2020:043D01. doi:10.1093/ptep/ptaa016

44. Li B-A, Magno M. Curvature-slope correlation of nuclear symmetry energy and its imprints on the crust-core transition, radius and tidal deformability of canonical neutron stars. *Phys Rev C* (2020) 102:045807. doi:10.1103/PhysRevC.102.045807

45. Lopes LL. Role of the symmetry energy slope in neutron stars: exploring the model dependency. *Phys Rev C* (2024) 110:015805. doi:10.1103/PhysRevC.110.015805

46. Lim Y, Schwenk A. Symmetry energy and neutron star properties constrained by chiral effective field theory calculations. *Phys Rev C* (2024) 109:035801. doi:10.1103/PhysRevC.109.035801

47. Adhikari D, Albataineh H, Androic D, Aniol K, Armstrong D, Averett T, et al. Accurate determination of the neutron skin thickness of ^{208}Pb through parity-violation in electron scattering. *Phys Rev Lett* (2021) 126:172502. doi:10.1103/PhysRevLett.126.172502

48. Reed BT, Fattoyev FJ, Horowitz CJ, Piekarewicz J. Implications of PREX-2 on the equation of state of neutron-rich matter. *Phys Rev Lett* (2021) 126:172503. doi:10.1103/PhysRevLett.126.172503

49. Reinhard P-G, Roca-Maza X, Nazarewicz W. Information content of the parity-violating asymmetry in Pb208. *Phys Rev Lett* (2021) 127:232501. doi:10.1103/PhysRevLett.127.232501

50. Adhikari D, Albataineh H, Androic D, Aniol K, Armstrong D, Averett T, et al. Precision determination of the neutral weak form factor of ^{48}Ca. *Phys Rev Lett* (2022) 129:042501. doi:10.1103/PhysRevLett.129.042501

51. Zenihiro J, Sakaguchi H, Murakami T, Yosoi M, Yasuda Y, Terashima S, et al. Neutron density distributions of Pb-204, Pb-206, Pb-208 deduced

via proton elastic scattering at Ep=295 MeV. *Phys Rev C* (2010) 82:044611. doi:10.1103/PhysRevC.82.044611

52. Tamii A, Poltoratska I, von Neumann-Cosel P, Fujita Y, Adachi T, Bertulani CA, et al. Complete electric dipole response and the neutron skin in 208Pb. *Phys Rev Lett* (2011) 107:062502. doi:10.1103/PhysRevLett.107.062502

53. Centelles M, Roca-Maza X, Vinas X, Warda M. Nuclear symmetry energy probed by neutron skin thickness of nuclei. *Phys Rev Lett* (2009) 102:122502. doi:10.1103/PhysRevLett.102.122502

54. Dutra M, Lourenço O, Avancini SS, Carlson BV, Delfino A, Menezes DP, et al. Relativistic mean-field hadronic models under nuclear matter constraints. *Phys Rev C* (2014) 90:055203. doi:10.1103/PhysRevC.90.055203

55. Trzcinska A, Jastrzebski J, Lubinski P, Hartmann FJ, Schmidt R, von Egidy T, et al. Neutron density distributions deduced from anti-protonic atoms. *Phys Rev Lett* (2001) 87:082501. doi:10.1103/PhysRevLett.87.082501

56. Zabari N, Kubis S, Wójcik W. Influence of the interactions of scalar mesons on the behavior of the symmetry energy. *Phys Rev C* (2019) 99:035209. doi:10.1103/PhysRevC.99.035209

57. Miyatsu T, Cheoun M-K, Saito K. Asymmetric nuclear matter in relativistic mean-field models with isoscalar- and isovector-meson mixing. *Astrophys J* (2022) 929:82. doi:10.3847/1538-4357/ac5f40

58. Miyatsu T, Cheoun M-K, Kim K, Saito K. Can the PREX-2 and CREX results be understood by relativistic mean-field models with the astrophysical constraints? *Phys Lett B* (2023) 843:138013. doi:10.1016/j.physletb.2023.138013

59. Li F, Cai B-J, Zhou Y, Jiang W-Z, Chen L-W. Effects of isoscalar- and isovector-scalar meson mixing on neutron star structure. *Astrophys J* (2022) 929:183. doi:10.3847/1538-4357/ac5e2a

60. Danielewicz P, Lacey R, Lynch WG. Determination of the equation of state of dense matter. *Science* (2002) 298:1592–6. doi:10.1126/science.1078070

61. Fuchs C. Kaon production in heavy ion reactions at intermediate energies. *Prog Part Nucl Phys* (2006) 56:1–103. doi:10.1016/j.ppnp.2005.07.004

62. Lynch WG, Tsang MB, Zhang Y, Danielewicz P, Famiano M, Li Z, et al. Probing the symmetry energy with heavy ions. *Prog Part Nucl Phys* (2009) 62:427–32. doi:10.1016/j.ppnp.2009.01.001

63. Oliinychenko D, Sorensen A, Koch V, McLerran L. Sensitivity of Au+Au collisions to the symmetric nuclear matter equation of state at 2–5 nuclear saturation densities. *Phys Rev C* (2023) 108:034908. doi:10.1103/PhysRevC.108.034908

64. Cromartie HT, Fonseca E, Ransom SM, Demorest PB, Arzoumanian Z, Blumer H, et al. Relativistic Shapiro delay measurements of an extremely massive millisecond pulsar. *Nat Astron* (2019) 4:72–6. doi:10.1038/s41550-019-0880-2

65. Fonseca E, Cromartie HT, Pennucci TT, Ray PS, Kirichenko AY, Ransom SM, et al. Refined mass and geometric measurements of the high-mass PSR J0740+6620. *Astrophys J Lett* (2021) 915:L12. doi:10.3847/2041-8213/ac03b8

66. Ring P. Relativistic mean field theory in finite nuclei. *Prog Part Nucl Phys* (1996) 37:193–263. doi:10.1016/0146-6410(96)00054-3

67. Lalazissis GA, Konig J, Ring P. A New parametrization for the Lagrangian density of relativistic mean field theory. *Phys Rev C* (1997) 55:540–3. doi:10.1103/PhysRevC.55.540

68. Pradhan BK, Chatterjee D, Gandhi R, Schaffner-Bielich J. Role of vector self-interaction in neutron star properties. *Nucl Phys A* (2023) 1030:122578. doi:10.1016/j.nuclphysa.2022.122578

69. Malik T, Dexheimer V, Providência C. Astrophysics and nuclear physics informed interactions in dense matter: inclusion of PSR J0437-4715. *Phys Rev D* (2024) 110:043042. doi:10.1103/PhysRevD.110.043042

70. Todd-Rutel BG, Piekarewicz J. Neutron-Rich nuclei and neutron stars: a new accurately calibrated interaction for the study of neutron-rich matter. *Phys Rev Lett* (2005) 95:122501. doi:10.1103/PhysRevLett.95.122501

71. Miyatsu T, Cheoun M-K, Saito K. Equation of state for neutron stars in SU(3) flavor symmetry. *Phys Rev C* (2013) 88:015802. doi:10.1103/PhysRevC.88.015802

72. Horowitz CJ, Piekarewicz J. Neutron star structure and the neutron radius of Pb-208. *Phys Rev Lett* (2001) 86:5647–50. doi:10.1103/PhysRevLett.86.5647

73. Haidari MM, Sharma MM. Sigma-omega meson coupling and properties of nuclei and nuclear matter. *Nucl Phys A* (2008) 803:159–72. doi:10.1016/j.nuclphysa.2008.02.296

74. Sharma MM. Scalar-vector Lagrangian without nonlinear self-interactions of bosonic fields in the relativistic mean-field theory. *Phys Lett B* (2008) 666:140–4. doi:10.1016/j.physletb.2008.07.005

75. Kubis S, Wójcik W, Castillo DA, Zabari N. Relativistic mean-field model for the ultracompact low-mass neutron star HESS J1731-347. *Phys Rev C* (2023) 108:045803. doi:10.1103/PhysRevC.108.045803

76. Chen L-W, Ko CM, Li B-A. Isospin-dependent properties of asymmetric nuclear matter in relativistic mean-field models. *Phys Rev C* (2007) 76:054316. doi:10.1103/PhysRevC.76.054316

77. Chen L-W, Cai B-J, Ko CM, Li B-A, Shen C, Xu J. Higher-order effects on the incompressibility of isospin asymmetric nuclear matter. *Phys Rev C* (2009) 80:014322. doi:10.1103/PhysRevC.80.014322

78. Czerski P, De Pace A, Molinari A. Revisiting the Hugenholtz-Van Hove theorem in nuclear matter. *Phys Rev C* (2002) 65:044317. doi:10.1103/PhysRevC.65.044317

79. Cai B-J, Chen L-W. Lorentz covariant nucleon self-energy decomposition of the nuclear symmetry energy. *Phys Lett B* (2012) 711:104–8. doi:10.1016/j.physletb.2012.03.058

80. Miyatsu T, Katayama T, Saito K. Effects of Fock term, tensor coupling and baryon structure variation on a neutron star. *Phys Lett B* (2012) 709:242–6. doi:10.1016/j.physletb.2012.02.009

81. Katayama T, Miyatsu T, Saito K. EoS for massive neutron stars. *Astrophys J Suppl* (2012) 203:22. doi:10.1088/0067-0049/203/2/22

82. Miyatsu T, Cheoun M-K, Ishizuka C, Kim KS, Maruyama T, Saito K. Decomposition of nuclear symmetry energy based on Lorentz-covariant nucleon self-energies in relativistic Hartree-Fock approximation. *Phys Lett B* (2020) 803:135282. doi:10.1016/j.physletb.2020.135282

83. Kubis S. Nuclear symmetry energy and stability of matter in neutron stars. *Phys Rev C* (2007) 76:025801. doi:10.1103/PhysRevC.76.025801

84. Lattimer JM, Prakash M. Neutron star observations: prognosis for equation of state constraints. *Phys Rept* (2007) 442:109–65. doi:10.1016/j.physrep.2007.02.003

85. Xu J, Chen L-W, Li B-A, Ma H-R. Nuclear constraints on properties of neutron star crusts. *Astrophys J* (2009) 697:1549–68. doi:10.1088/0004-637X/697/2/1549

86. Moustakidis CC, Niksic T, Lalazissis GA, Vretenar D, Ring P. Constraints on the inner edge of neutron star crusts from relativistic nuclear energy density functionals. *Phys Rev C* (2010) 81:065803. doi:10.1103/PhysRevC.81.065803

87. Psonis VP, Moustakidis CC, Massen SE. Nuclear symmetry energy effects on neutron stars properties. *Mod Phys Lett A* (2007) 22:1233–53. doi:10.1142/S0217732307023572

88. Kubis S, Wójcik W, Zabari N. Multilayer neutron stars with scalar mesons crossing term. *Phys Rev C* (2020) 102:065803. doi:10.1103/PhysRevC.102.065803

89. Routray TR, Viñas X, Basu DN, Pattnaik SP, Centelles M, Robledo L, et al. Exact versus Taylor-expanded energy density in the study of the neutron star crust–core transition. *J Phys G* (2016) 43:105101. doi:10.1088/0954-3899/43/10/105101

90. Zhang N-B, Li B-A, Xu J. Combined constraints on the equation of state of dense neutron-rich matter from terrestrial nuclear experiments and observations of neutron stars. *Astrophys J* (2018) 859:90. doi:10.3847/1538-4357/aac027

91. Xie W-J, Li B-A. Bayesian inference of high-density nuclear symmetry energy from radii of canonical neutron stars. *Astrophys J* (2019) 883:174. doi:10.3847/1538-4357/ab3f37

92. Miyatsu T, Cheoun M-K, Kim K, Saito K. Massive neutron stars with small radii in relativistic mean-field models optimized to nuclear ground states. *Preprint arXiv:2209.02861* (2022) [nucl–th]. doi:10.48550/arXiv.2209.02861

93. Abbott R, Abbott TD, Abraham S, Acernese F, Ackley K, Adams C, et al. GW190814: gravitational waves from the coalescence of a 23 solar mass black hole with a 2.6 solar mass compact object. *Astrophys J Lett* (2020) 896:L44. doi:10.3847/2041-8213/ab960f

94. Fattoyev FJ, Horowitz CJ, Piekarewicz J, Reed B. GW190814: impact of a 2.6 solar mass neutron star on the nucleonic equations of state. *Phys Rev C* (2020) 102:065805. doi:10.1103/PhysRevC.102.065805

95. Reed BT, Fattoyev FJ, Horowitz CJ, Piekarewicz J. Density dependence of the symmetry energy in the post–PREX-CREX era. *Phys Rev C* (2024) 109:035803. doi:10.1103/PhysRevC.109.035803

96. Chen W-C, Piekarewicz J. Searching for isovector signatures in the neutron-rich oxygen and calcium isotopes. *Phys Lett B* (2015) 748:284–8. doi:10.1016/j.physletb.2015.07.020

97. Fattoyev FJ, Piekarewicz J. Sensitivity of the moment of inertia of neutron stars to the equation of state of neutron-rich matter. *Phys Rev C* (2010) 82:025810. doi:10.1103/PhysRevC.82.025810

98. Chen W-C, Piekarewicz J. Building relativistic mean field models for finite nuclei and neutron stars. *Phys Rev C* (2014) 90:044305. doi:10.1103/PhysRevC.90.044305

99. Salinas M, Piekarewicz J. Bayesian refinement of covariant energy density functionals. *Phys Rev C* (2023) 107:045802. doi:10.1103/PhysRevC.107.045802

100. Salinas M, Piekarewicz J. Building an equation of state density ladder. *Symmetry* (2023) 15:994. doi:10.3390/sym15050994

101. Kumar S, Kumar M, Kumar R, Dhiman SK. Implications of isoscalar and isovector scalar meson mixed interaction on nuclear and neutron star properties. *Phys Rev C* (2023) 108:055802. doi:10.1103/PhysRevC.108.055802

102. Kumar B, Agrawal BK, Patra SK. New relativistic effective interaction for finite nuclei, infinite nuclear matter and neutron stars. *Phys Rev C* (2018) 97:045806. doi:10.1103/PhysRevC.97.045806

103. Fattoyev FJ, Horowitz CJ, Piekarewicz J, Shen G. Relativistic effective interaction for nuclei, giant resonances, and neutron stars. *Phys Rev C* (2010) 82:055803. doi:10.1103/PhysRevC.82.055803

104. Liliani N, Diningrum JP, Sulaksono A. Tensor and Coulomb-exchange terms in the relativistic mean-field model with δ-meson and isoscalar-isovector coupling. *Phys Rev C* (2021) 104:015804. doi:10.1103/PhysRevC.104.015804

105. Fattoyev FJ, Piekarewicz J. Has a thick neutron skin in ^{208}Pb been ruled out? *Phys Rev Lett* (2013) 111:162501. doi:10.1103/PhysRevLett.111.162501

106. Piekarewicz J. Symmetry energy constraints from giant resonances: a theoretical overview. *Eur Phys J* (2014) A 50:25. doi:10.1140/epja/i2014-14025-x

107. Birkhan J, Miorelli M, Bacca S, Bassauer S, Bertulani C, Hagen G, et al. Electric dipole polarizability of ^{48}Ca and implications for the neutron skin. *Phys Rev Lett* (2017) 118:252501. doi:10.1103/PhysRevLett.118.252501

108. Tarbert CM, Watts D, Glazier D, Aguar P, Ahrens J, Annand J, et al. Neutron skin of ^{208}Pb from coherent pion photoproduction. *Phys Rev Lett* (2014) 112:242502. doi:10.1103/PhysRevLett.112.242502

109. Reinhard PG, Rufa M, Maruhn J, Greiner W, Friedrich J. Nuclear ground state properties in a relativistic meson field theory. *Z Phys A* (1986) 323:13–25. doi:10.1007/bf01294551

110. Liliani N, Nugraha AM, Diningrum JP, Sulaksono A. Tensor and isovector–isoscalar terms of relativistic mean field model: impacts on neutron-skin thickness, charge radius, and nuclear matter. *Nucl Phys A* (2024) 1042:122812. doi:10.1016/j.nuclphysa.2023.122812

111. De Vries H, De Jager CW, De Vries C. Nuclear charge-density-distribution parameters from elastic electron scattering. *Atom Data Nucl Data Tabl* (1987) 36:495–536. doi:10.1016/0092-640X(87)90013-1

112. Horowitz CJ, Pollock SJ, Souder PA, Michaels R. Parity violating measurements of neutron densities. *Phys Rev C* (2001) 63:025501. doi:10.1103/PhysRevC.63.025501

113. Horowitz CJ, Ahmed Z, Jen CM, Rakhman A, Souder PA, Dalton MM, et al. Weak charge form factor and radius of 208Pb through parity violation in electron scattering. *Phys Rev C* (2012) 85:032501. doi:10.1103/PhysRevC.85.032501

114. Niksic T, Vretenar D, Finelli P, Ring P. Relativistic Hartree-Bogoliubov model with density-dependent meson-nucleon couplings. *Phys Rev C* (2002) 66:024306. doi:10.1103/PhysRevC.66.024306

115. Ma Y-L, Rho M. Topology change, emergent symmetries and compact star matter. *AAPPS Bull* (2021) 31:16. doi:10.1007/s43673-021-00016-1

116. Lee HK, Ma Y-L, Paeng W-G, Rho M. Cusp in the symmetry energy, speed of sound in neutron stars and emergent pseudo-conformal symmetry. *Mod Phys Lett A* (2022) 37:2230003. doi:10.1142/S0217732322300038

117. Chen L-W, Ko CM, Li B-A. Nuclear matter symmetry energy and the neutron skin thickness of heavy nuclei. *Phys Rev C* (2005) 72:064309. doi:10.1103/PhysRevC.72.064309

118. Maruyama T, Chiba S. Equation of state of neutron star matter and the isovector nucleon optical model potential. *J Phys G* (1999) 25:2361–9. doi:10.1088/0954-3899/25/12/306

119. Maruyama T, Balantekin AB, Cheoun M-K, Kajino T, Kusakabe M, Mathews GJ. A relativistic quantum approach to neutrino and antineutrino emission via the direct Urca process in strongly magnetized neutron-star matter. *Phys Lett B* (2022) 824:136813. doi:10.1016/j.physletb.2021.136813

120. Glendenning NK (1997) Compact stars: nuclear physics, particle physics, and general relativity

121. Miyatsu T, Yamamuro S, Nakazato K. A new equation of state for neutron star matter with nuclei in the crust and hyperons in the core. *Astrophys J* (2013) 777:4. doi:10.1088/0004-637X/777/1/4

122. Miyatsu T, Cheoun M-K, Saito K. Equation of state for neutron stars with hyperons and quarks in the relativistic Hartree–Fock approximation. *Astrophys J* (2015) 813:135. doi:10.1088/0004-637X/813/2/135

123. Tolman RC. Static solutions of Einstein's field equations for spheres of fluid. *Phys Rev* (1939) 55:364–73. doi:10.1103/PhysRev.55.364

124. Oppenheimer JR, Volkoff GM. On massive neutron cores. *Phys Rev* (1939) 55:374–81. doi:10.1103/PhysRev.55.374

125. Sulaksono A, Alam N, Agrawal BK. Core–crust transition properties of neutron stars within systematically varied extended relativistic mean-field model. *Int J Mod Phys E* (2014) 23:1450072. doi:10.1142/S0218301314500724

126. Providência C, Avancini SS, Cavagnoli R, Chiacchiera S, Ducoin C, Grill F, et al. Imprint of the symmetry energy on the inner crust and strangeness content of neutron stars. *Eur Phys J* (2014) A 50:44. doi:10.1140/epja/i2014-14044-7

127. Li B-A, Krastev PG, Wen D-H, Zhang N-B. Towards understanding astrophysical effects of nuclear symmetry energy. *Eur Phys J* (2019) A 55:117. doi:10.1140/epja/i2019-12780-8

128. Horowitz CJ, Piekarewicz J. Constraining URCA cooling of neutron stars from the neutron radius of Pb-208. *Phys Rev C* (2002) 66:055803. doi:10.1103/PhysRevC.66.055803

129. Page D, Geppert U, Weber F. The Cooling of compact stars. *Nucl Phys A* (2006) 777:497–530. doi:10.1016/j.nuclphysa.2005.09.019

130. Lattimer JM, Prakash M, Pethick CJ, Haensel P. Direct URCA process in neutron stars. *Phys Rev Lett* (1991) 66:2701–4. doi:10.1103/PhysRevLett.66.2701

131. Rutherford N, Mendes M, Svensson I, Schwenk A, Watts AL, Hebeler K, et al. Constraining the dense matter equation of state with new NICER mass–radius measurements and new chiral effective field theory inputs. *Astrophys J Lett* (2024) 971:L19. doi:10.3847/2041-8213/ad5f02

132. Choudhury D, Salmi T, Vinciguerra S, Riley TE, Kini Y, Watts AL, et al. A NICER view of the nearest and brightest millisecond pulsar: PSR J0437–4715. *Astrophys J Lett* (2024) 971:L20. doi:10.3847/2041-8213/ad5a6f

133. Guichon PAM. A possible quark mechanism for the saturation of nuclear matter. *Phys Lett B* (1988) 200:235–40. doi:10.1016/0370-2693(88)90762-9

134. Saito K, Thomas AW. A Quark - meson coupling model for nuclear and neutron matter. *Phys Lett B* (1994) 327:9–16. doi:10.1016/0370-2693(94)91520-2

135. Saito K, Thomas AW. The Nolen-Schiffer anomaly and isospin symmetry breaking in nuclear matter. *Phys Lett B* (1994) 335:17–23. doi:10.1016/0370-2693(94)91551-2

136. Saito K, Tsushima K, Thomas AW. Nucleon and hadron structure changes in the nuclear medium and the impact on observables. *Prog Part Nucl Phys* (2007) 58:1–167. doi:10.1016/j.ppnp.2005.07.003

137. Saito K, Miyatsu T, Cheoun M-K. Effect of isoscalar and isovector scalar fields on baryon semileptonic decays in nuclear matter. *Phys Rev D* (2024) 110:113001. doi:10.1103/PhysRevD.110.113001

138. Nagai S, Miyatsu T, Saito K, Tsushima K. Quark-meson coupling model with the cloudy bag. *Phys Lett B* (2008) 666:239–44. doi:10.1016/j.physletb.2008.07.065

139. Chen L-W, Ko CM, Li B-A. Determination of the stiffness of the nuclear symmetry energy from isospin diffusion. *Phys Rev Lett* (2005) 94:032701. doi:10.1103/PhysRevLett.94.032701

140. Li B-A, Chen L-W. Nucleon-nucleon cross sections in neutron-rich matter and isospin transport in heavy-ion reactions at intermediate energies. *Phys Rev C* (2005) 72:064611. doi:10.1103/PhysRevC.72.064611

141. Estee J, Lynch W, Tsang C, Barney J, Jhang G, Tsang M, et al. Probing the symmetry energy with the spectral pion ratio. *Phys Rev Lett* (2021) 126:162701. doi:10.1103/PhysRevLett.126.162701

142. Lynch WG, Tsang MB. Decoding the density dependence of the nuclear symmetry energy. *Phys Lett B* (2022) 830:137098. doi:10.1016/j.physletb.2022.137098

143. Tsang CY, Tsang MB, Lynch WG, Kumar R, Horowitz CJ. Determination of the equation of state from nuclear experiments and neutron star observations. *Nat Astron* (2024) 8:328–36. doi:10.1038/s41550-023-02161-z

144. Chen L-W. Symmetry energy systematics and its high density behavior. *EPJ Web Conf* (2015) 88:00017. doi:10.1051/epjconf/20158800017

145. Li B-A, Cai B-J, Xie W-J, Zhang N-B. Progress in constraining nuclear symmetry energy using neutron star observables since GW170817. *Universe* (2021) 7:182. doi:10.3390/universe7060182

146. Negele JW, Vautherin D. Neutron star matter at subnuclear densities. *Nucl Phys A* (1973) 207:298–320. doi:10.1016/0375-9474(73)90349-7

147. Sotani H, Ota S. Neutron star mass formula with nuclear saturation parameters for asymmetric nuclear matter. *Phys Rev D* (2022) 106:103005. doi:10.1103/PhysRevD.106.103005

148. Lattimer JM. Constraints on nuclear symmetry energy parameters. *Particles* (2023) 6:30–56. doi:10.3390/particles6010003